










## High precision measurement of the $^{99}\text{Tc}$ $\beta$ spectrum

M. Paulsen <sup>1,2,\*</sup> P. C.-O. Ranitzsch,<sup>3,†</sup> M. Loidl <sup>4</sup> M. Rodrigues <sup>4</sup> K. Kossert,<sup>3</sup> X. Mougeot <sup>4,‡</sup> A. Singh,<sup>4,§</sup> S. Leblond <sup>4</sup> J. Beyer,<sup>1</sup> L. Bockhorn <sup>3,||</sup> C. Enss,<sup>2</sup> M. Wegner <sup>5,6</sup> S. Kempf <sup>6,5</sup> and O. Nähle <sup>3</sup>

<sup>1</sup>Physikalisch-Technische Bundesanstalt Berlin, Abbestraße 2-12, 10587 Berlin, Germany

<sup>2</sup>Kirchhoff-Institute for Physics, Im Neuenheimer Feld 227, 69120 Heidelberg, Germany

<sup>3</sup>Physikalisch-Technische Bundesanstalt Braunschweig, Bundesallee 100, 38116 Braunschweig, Germany

<sup>4</sup>Université Paris-Saclay, CEA, List, Laboratoire National Henri Becquerel (LNE-LNHB), F-91120 Palaiseau, France

<sup>5</sup>Institute for Data Processing and Electronics (IPE), Karlsruhe Institute of Technology (KIT),

Hermann-von-Helmholtz-Platz 1, 76344 Eggenstein-Leopoldshafen, Germany

<sup>6</sup>Institute of Micro- and Nanoelectronic Systems (IMS), Karlsruhe Institute of Technology (KIT), Hertzstraße 16, 76187 Karlsruhe, Germany



(Received 5 October 2023; revised 16 August 2024; accepted 22 October 2024; published 20 November 2024)

Highly precise measurements of the  $^{99}\text{Tc}$   $\beta$  spectrum were performed in two laboratories using metallic magnetic calorimeters. Independent sample preparations, evaluation methods, and analyses yielded consistent results and the spectrum could be measured down to less than 1 keV. Consistent  $\beta$  spectra were also obtained via cross evaluations of the experimental data sets. An additional independent measurement with silicon detectors in a  $4\pi$  configuration confirms the spectrum shape above 25 keV. Detailed theoretical calculations were performed using the nuclear shell model and including atomic effects. The spectrum shape was found to be sensitive to the effective value of the axial-vector coupling constant. Combining measurements and predictions, we extracted  $Q_\beta = 295.82(16)$  keV,  $g_V^{\text{eff}} = 0.376(5)$ , and  $g_A^{\text{eff}} = 0.574(36)$ , which seems to solve an inconsistency of the quenched coupling constants between first and higher forbidden nonunique transitions. Furthermore, we derived the mean energy of the  $\beta$  spectrum,  $\bar{E}_\beta = 98.51(23)$  keV,  $\log f = -0.47660(22)$ , and  $\log ft = 12.3478(23)$ .

DOI: [10.1103/PhysRevC.110.055503](https://doi.org/10.1103/PhysRevC.110.055503)

### I. INTRODUCTION

$\beta$  spectrometry, the precise shape of  $\beta$  spectra, and their theoretical description have received increased interest recently from different research fields, e.g., radionuclide metrology [1–3], neutrino physics [4–6], and nuclear theory [7–9]. In the context of radionuclide metrology, the European metrology research project MetroBeta [10] (2016–2019) addressed the precise measurement and theoretical calculation of several  $\beta$  spectra.

The ground state of  $^{99}\text{Tc}$  decays mainly via pure  $\beta$  emission [ $\beta^-$ , 99.998 55(30)%] to the  $^{99}\text{Ru}$  ground state [11]; see Fig. 1. The spectrum shape of this second forbidden nonunique transition has been measured several times using

magnetic [12,13], scintillation [14], and semiconductor [15] spectrometers [16]. While these setups corresponded to the state of the art when they were applied in the 1950–1970s, the measurements suffer from rather high energy thresholds ( $>50$  keV) and it is expected that one can achieve significantly higher energy resolution with present-day methods. In addition, the  $\beta$  spectrum shape of  $^{99}\text{Tc}$  has recently been predicted in [8] to be very sensitive to the effective value of the weak interaction axial-vector coupling constant  $g_A$ , making its high precision measurement very interesting. The currently accepted  $Q$ -value 297.5(9) keV [17] has a relative standard uncertainty of about 0.3%. The value is mainly influenced by Alburger *et al.* [18] who used an iron-free intermediate-image magnetic spectrometer to measure the decay energies of  $^{99m}\text{Tc}$ . Modern methods such as Penning traps or cryogenic microcalorimeters, as presented here, allow for more accurate measurements.

The achieved result for the average  $\beta$  energy of  $^{99}\text{Tc}$  has a direct application for calculating nuclear reactor models and radioactive waste management. In a recent study, the influence of nuclear data on decay heat from spent nuclear fuel over a period of 1 to  $10^5$  years was assessed [19]. A list of the most significant contributing radionuclides was provided.  $^{99}\text{Tc}$  was placed at the very top, with an average  $\beta$  energy that ranges from 84 to 95 keV and a stated uncertainty of less than 1%, depending on the data library.

In the framework of the MetroBeta project, a  $\beta$  spectrum of  $^{99}\text{Tc}$  was measured with metallic magnetic calorimeters

\*Contact author: michael.paulsen@ptb.de

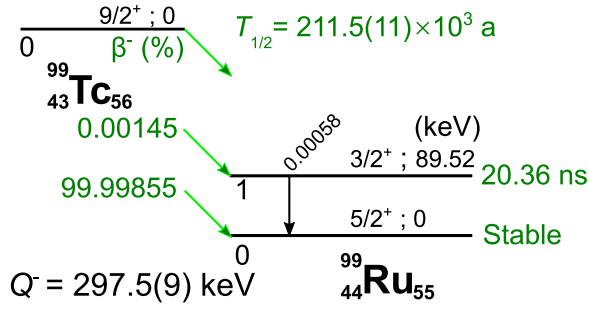
<sup>†</sup>Present address: Deutsches Zentrum für Luft-und Raumfahrt e.V. Hamburg, Hamburg, Germany.

<sup>‡</sup>Contact author: xavier.mougeot@cea.fr

<sup>§</sup>Present address: Physikalisch-Technische Bundesanstalt Braunschweig, Bundesallee 100, 38116 Braunschweig, Germany.

<sup>||</sup>Present address: Institut für Festkörperphysik, Leibniz Universität Hannover, Appelstraße 2, 30167 Hannover, Germany.

Published by the American Physical Society under the terms of the [Creative Commons Attribution 4.0 International](https://creativecommons.org/licenses/by/4.0/) license. Further distribution of this work must maintain attribution to the author(s) and the published article's title, journal citation, and DOI.

FIG. 1. Decay scheme of  $^{99}\text{Tc}$ .

(MMCs), which was first presented in [20,21]. It featured two-orders-of-magnitude-lower energy thresholds (0.65 keV) and a greatly improved energy resolution (0.1 keV at 383 keV) compared to previous measurements. The spectrum was obtained at the Laboratoire National Henri Becquerel (LNHB) and shows excellent agreement with a corresponding measurement at the Physikalisch-Technische Bundesanstalt (PTB) using a similar MMC setup, which confirms the spectrum shape over the entire energy range. At energies above 25 keV, the spectrum shapes are further confirmed with a state-of-the-art passivated implanted planar silicon (PIPS) detector measurement, also performed at LNHB.

The remainder of the paper is organized as depicted in Fig. 2. In Sec. II, we report on the three independent measurements of the  $^{99}\text{Tc}$   $\beta$  spectrum and on the data analyses performed to correct for small, but relevant distortions due to the detection systems. We next discuss theory in Sec. III that connects these accurate measurements with detailed theoretical predictions in order to extract the  $^{99}\text{Tc}$   $Q$ -value and the effective  $g_A$  coupling constant using the spectrum-shape method. The average energy of the  $\beta$  spectrum  $\bar{E}_\beta$  and the  $\log f$  value are derived from the resulting theoretical spectrum. A qualitative comparison of all three measurements with the currently recommended spectrum [15] confirms our findings.

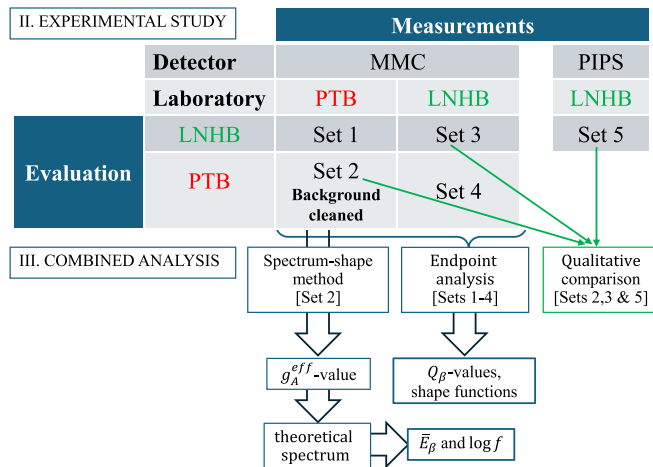


FIG. 2. Schematic overview of the data, evaluation, and analysis of this work.

TABLE I. Setup properties of the MMC experiments at the LNHB and PTB laboratories. The values for the input inductance and heat capacity are nominal per fabrication and calculated values, respectively.

Laboratory	LNHB [10,20,21]	PTB [28,29]
Cryostat	$^3\text{He}$ dilution insert in $^4\text{He}$ (l) bath for precooling	$^3\text{He}$ dilution refrigerator with two stage pulse tube for precooling
MMC chip	MetroBeta V1-M [10]	MetroBeta V2-M [29]
SQUID chip	Supracon VC1A input inductance 4.5 nH	PTB X1 input inductance 2 nH
Absorber	Au, heat capacity 350 pJ/K at 20 mK matched to MMC chip	Au, heat capacity 112 pJ/K at 20 mK matched to MMC chip
Sample	electrodeposited	drop deposited
Calibration source	$^{133}\text{Ba}$	$^{57}\text{Co}$
Analysis code	Optimal filtering in MATLAB	Optimal filtering in PYTHON

## II. EXPERIMENTAL STUDY

### A. MMC measurements

MMCs [22–24] are cryogenic microcalorimeters that consist of a—mostly metallic—particle absorber in strong thermal contact with a metallic paramagnet (here,  $\text{Ag:Er}_{300\text{ppm}}$ ) acting as a temperature sensor. The paramagnet is placed in a weak magnetic field ( $\approx 10$  mT) and operated at temperatures  $< 100$  mK. When an energy  $E$  is deposited into the absorber, it leads to a temperature increase  $\Delta T$ . As the magnetic susceptibility of the paramagnet has a strong temperature dependence, the temperature increase causes a change in its magnetization,

$$\Delta M = \frac{\partial M}{\partial T} \cdot \Delta T = \frac{\partial M}{\partial T} \cdot \frac{E}{C_{\text{tot}}}, \quad (1)$$

where  $C_{\text{tot}}$  denotes the total heat capacity of the absorber and the paramagnet. A superconducting coil coupled to the paramagnet picks up the change in magnetization as a corresponding magnetic flux change  $\Delta \Phi$ , which is measured with a superconducting quantum interference device (SQUID) [25].

Setups using MMCs with the radionuclide source embedded in a  $4\pi$  solid angle absorber geometry have proven to be among the best  $\beta$  spectrometers in terms of energy resolution and energy threshold, in particular for low-energy  $\beta$  transitions [20,21,26,27]. Both measurements presented here follow that approach, but the technical realization differs in many details. These are summarized in Table I and described in the following.

### 1. Setup and analysis (LNHB)

The starting point of the detector fabrication at LNHB was the source preparation. Following a protocol yielding metallic technetium [30],  $^{99}\text{Tc}$  was electrodeposited onto a 10- $\mu\text{m}$ -thick gold foil. The foil was then rinsed with water in order to remove salt having crystallized from the  $^{99}\text{Tc}$  solution on the

foil. Some visible salt deposit remained even after rinsing, but in an autoradiographic image of the source, several areas without any salt deposit but with a presence of  $^{99}\text{Tc}$  activity were found. The electrodeposition yield was low and an area of the source foil larger than the typical size of MMC absorbers had to be used to have sufficient activity in the MMC absorber. The selected piece of source foil ( $\approx 0.9 \times 2.5$  mm) with a transparently thin metallic  $^{99}\text{Tc}$  deposit was folded three times to reduce it to a small enough size ( $\approx 0.44 \times 0.64 \times 54$  mm) such that it could be enclosed into the MMC absorber. The folded foil with a  $^{99}\text{Tc}$  activity of  $\approx 5$  Bq was sandwiched between two gold foils ( $0.9 \times 0.9 \times 74$  mm each) and this stack was diffusion welded. Since the source carrier foil and absorber foils are made of gold and diffusion welded, the source foil with the embedded activity forms part of the final absorber, both geometrically and thermally. This means that if the radiation deposits its energy in the source foil or the absorber foil, it results in equivalent signals. The final absorber had a heat capacity of  $\approx 350$  pJ/K at 20 mK and was glued with Stycast 1266 epoxy to one of the pixels of a MetroBeta V1 M-sized MMC chip [10].

Due to the continuous nature of the  $\beta$  spectra, without any distinct features, energy calibration is essential, in particular if the end point energy is to be determined from an experimental spectrum. To precisely determine the spectrum shape, checking and correcting for any nonlinearities in energy is also important. A common way to perform energy calibration is to use x-ray and/or gamma ray photons of well-known energies from an external radionuclide source collimated onto the detector. To cover the full energy range of the  $^{99}\text{Tc}$   $\beta$  spectrum, at LNHB a  $^{133}\text{Ba}$  source of approximately 50 kBq was chosen. It emits x-ray and gamma lines between 30.63 and 383.85 keV. The conversion electrons that are also emitted are stopped in a 100- $\mu\text{m}$ -thick aluminum foil placed between the source and the collimator. The  $^{133}\text{Ba}$  source was placed at a distance of 31 mm from the absorber surface. A lead collimator was composed of a 8-mm-thick top part with a 1 mm bore and a 2 mm thick bottom part with a 200  $\mu\text{m}$  bore placed at 2.5 mm from the absorber surface. The MMC signal was read out by a Supracon VC1A SQUID linked to a Magnicon XXF-1 electronics.

The whole setup was shielded against stray magnetic fields by means of a lead cylinder and operated in a liquid helium precooled  $^3\text{He}$  dilution refrigerator (Cryoconcept) at  $T = 12$  mK. Data were acquired as a continuous stream over 13.7 days at 100 kS/s; anti-aliasing filtering was set to 30 kHz on a Stanford Research Systems SRS 560 amplifier.

Pulses were triggered in the data stream offline, using a narrow band-pass filter. To minimize pile-up, an extendable dead time was applied. Once the pulse positions were determined, the pulse heights were estimated from raw data using an optimal filter in a MATLAB [31] environment. Slow variations of the pulse heights for a given energy due to temperature drifts of the cryostat were removed by fitting the pulse height-vs-time distribution for one densely populated line with a spline function and applying this fit function to all pulse heights. Spurious pulses were discriminated based on the pulse shapes in a  $\chi$ -square-vs-pulse-height plot. By correcting for temporal and magnetic fluctuations of the detector,

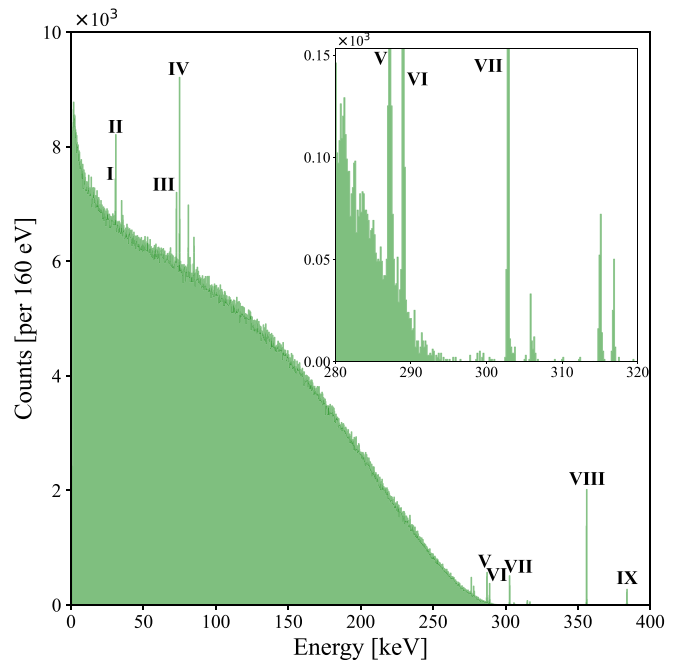


FIG. 3. Measured and calibrated LNHB MMC spectrum of  $^{99}\text{Tc}$  with  $^{133}\text{Ba}$  external source peaks of which nine were used for calibration: x-ray lines at 30.63 keV, 30.97 keV (denoted I, II: directly from the  $^{133}\text{Ba}$  source); 72.80 keV, 74.97 keV (denoted III, IV: Pb fluorescence from the setup material); escape lines at 287.21 keV, 289.02 keV (denoted V, VI: Au photons escape the absorber, generated by  $\gamma$  rays from the  $^{133}\text{Ba}$  source); and  $\gamma$  rays at 302.85 keV, 356.01 keV, 383.85 keV (denoted VII, VIII, IX: directly from the  $^{133}\text{Ba}$  source). Please see Table III for further details. Inset: Spectrum and background around the maximum  $\beta$  energy.

the systematic error of the experiment is decreased and the resulting energy resolution is improved. The final spectrum contains 7 264 451 events and is presented in Fig. 3.

The energy resolution is constant over the entire energy range,  $\Delta E \approx 100$  eV up to 384 keV. The linearity in energy was checked using the lines annotated in Fig. 3 and listed in Table III. Three line types were considered: (i)  $\gamma$  lines and x rays that originate directly from the calibration source, (ii) fluorescent lines due to secondary effects when the calibration source particles impact on the aluminum, gold, and lead components of the experimental setup, and (iii) escape lines which emerge when an atom in the gold absorber is hit by a photon of energy  $E$  from the calibration source. This creates

TABLE II. Polynomial calibration coefficients for the LNHB (Set 3) and PTB (Set 2) measurements using the calibration lines of Table III.

	LNHB (Set 3)	PTB (Set 2)
Calibration line (keV), $E_{\gamma}^{\text{lit}}$	356.012900	122.06065
Linear coefficient (keV), $k_1$	355.822	121.355
Quadratic coefficient (keV), $k_2$	0.183	0.706
Linearity offset, $\frac{E_{\gamma}^{\text{lit}}}{k_1} - 1$	0.1%	0.6%

TABLE III. Photon and escape lines used to check and correct for energy nonlinearity.

LNHB measurement						
Origin	Tabulated energy (keV)	Measured energy (keV)	$\Delta E$ (Set 3) (keV)	Radiation type	Calibration line: For Sets	
$^{133}\text{Ba}$ calibration source	30.63	30.61	-0.02	Cs X $K_{\alpha 2}$	I: 3,4	
	30.97	30.97	0	Cs X $K_{\alpha 1}$	II: 3,4	
	35.05	34.98	-0.07	Cs X $K_{\beta}$		
	81.00	81.06	0.06	$\gamma$		
	276.40	276.46	0.06	$\gamma$		
	302.85	302.88	0.00	$\gamma$	VII: 3,4	
	356.01	356.01	0	$\gamma$	VIII: 3,4	
	383.85	383.82	-0.03	$\gamma$	IX: 3,4	
Au/Pb fluorescence from setup/collimator	66.99	66.98	-0.01	Au X $K_{\alpha 2}$		
	68.80	68.78	-0.02	Au X $K_{\alpha 1}$		
	72.81	72.82	0.02	Pb X $K_{\alpha 2}$	III: 3,4	
	74.97	74.98	0.01	Pb X $K_{\alpha 1}$	IV: 3,4	
	84.94	84.98	0.04	Pb X $K_{\beta 1}$		
Escape lines				Gamma line (keV)	Escaping photon (keV)	
	278.03	278.07	0.04	356.01 [ $^{133}\text{Ba}$ $\gamma$ ]	77.98 [Au $K_{\beta 1}$ ]	
	278.43	278.54	0.11	356.01 [ $^{133}\text{Ba}$ $\gamma$ ]	77.58 [Au $K_{\beta 3}$ ]	
	287.21	287.28	0.07	356.01 [ $^{133}\text{Ba}$ $\gamma$ ]	68.80 [Au $K_{\alpha 1}$ ]	V:3,4
	289.02	289.08	0.06	356.01 [ $^{133}\text{Ba}$ $\gamma$ ]	66.99 [Au $K_{\alpha 2}$ ]	VI: 3,4
	305.86	305.92	0.06	383.85 [ $^{133}\text{Ba}$ $\gamma$ ]	77.98 [Au $K_{\beta 1}$ ]	
	315.05	315.08	0.03	383.85 [ $^{133}\text{Ba}$ $\gamma$ ]	68.80 [Au $K_{\alpha 1}$ ]	
316.85	316.91	0.05	383.85 [ $^{133}\text{Ba}$ $\gamma$ ]	66.99 [Au $K_{\alpha 2}$ ]		
PTB measurement						
Origin	Tabulated energy (keV)	Measured energy (keV)	$\Delta E$ (Set 2) (keV)	Radiation type	Calibration line: For Sets	
$^{57}\text{Co}$ calibration source	14.42	14.44	-0.02	$\gamma$		
	122.06	122.06	0.00	$\gamma$	VI: 1,2	
	136.47	136.38	0.09	$\gamma$	VII: 1,2	
Au/Pb fluorescence from setup/collimator	66.99	67.07	-0.08	Au X $K_{\alpha 2}$		
	68.80	68.95	-0.15	Au X $K_{\alpha 1}$		
	72.81	72.98	-0.17	Pb X $K_{\alpha 2}$	IV: 1,2	
	74.97	75.14	-0.17	Pb X $K_{\alpha 1}$	V: 1,2	
	84.94	85.09	-0.15	Pb X $K_{\beta 1}$		
Escape lines				Gamma/fluorescent line (keV)	Escaping photon (keV)	
	6.47	6.44	0.03	84.45 [Pb $K_{\beta 3}$ ]	77.98 [Au $K_{\beta 1}$ ]	
	6.96	6.97	-0.01	84.94 [Pb $K_{\beta 1}$ ]	77.98 [Au $K_{\beta 1}$ ]	
	16.13	16.22	-0.08	84.94 [Pb $K_{\beta 1}$ ]	68.80 [Au $K_{\alpha 1}$ ]	I: 1,2
	53.26	53.42	-0.17	122.06 [ $^{57}\text{Co}$ $\gamma$ ]	68.80 [Au $K_{\alpha 1}$ ]	II: 1,2
	55.07	55.24	-0.17	122.06 [ $^{57}\text{Co}$ $\gamma$ ]	66.99 [Au $K_{\alpha 2}$ ]	III: 1,2

a hole in the electronic shell of the gold atom that can be filled with an electron that transitions from an electron shell of higher energy. Then, a photon of energy  $E_{\text{Au}}^{\text{ph}}$  is emitted and, if it escapes the absorber, the energy  $E - E_{\text{Au}}^{\text{ph}}$  is absorbed instead.

First the energy scale was set uniquely using the 356.01 keV line, an intense  $\gamma$  line of the  $^{133}\text{Ba}$  calibration source lying beyond the endpoint of the  $^{99}\text{Tc}$   $\beta$  spectrum. Then the resulting energies of the other lines from the MMC measurement were compared with the recommended

energies [32], where, for the escape lines, the x-ray transition energies from [33] were used. The differences in energy between the tabulated and measured energies are all smaller or equal to the energy resolution; for the 30.97 keV line, the most intense x-ray line, it is zero. There is no clear trend in the difference between tabulated and measured energies as a function of energy, but it could be described with a second-order polynomial, as provided in Table II. This polynomial was then used to correct the energy scale for nonlinear effects. The values were achieved by making a quadratic ansatz using

the fit function,

$$E_i^{\text{lit}} = f^{\text{fit}}(a_i) := k_1 \cdot a_i + k_2 \cdot a_i^2$$

for  $i \in \{I, \dots, N\}$  and  $N \in \{VII, IX\}$ . (2)

$E_i^{\text{lit}}$  denotes the reference literature value of the respective peak and  $a_i := \frac{E_i^{\text{exp}}}{E_{\gamma}^{\text{lit}}}$  is the amplitude value of the detector, which corresponds to the pulse energy of the Gaussian fitted calibration line.  $E_i^{\text{exp}}$  denotes the measured experimental energy and  $E_{\gamma}^{\text{lit}}$  is the reference calibration energy used for a first energy calibration to set the energy scale, as the detector output is in units of voltage. The goal of the fit is to determine the coefficients  $k_1$  and  $k_2$ . Clearly, for a perfectly linear detector  $k_1 = E_{\gamma}^{\text{lit}}$ ,  $k_2 = 0$  and the linearity offset would be 0%. Here, the quadratic part was rather small and, in terms of the linearity offset, it was 0.1% and 0.6% in the LNHB and PTB experiment, respectively. The difference is due to the distinct designs, fabrications, and thermalizations of the MMC detectors.

## 2. Setup and analysis (PTB)

The measurement setup at PTB is functionally the same as at LNHB, but differs in several details. The difference with possibly the largest influence on the measured spectrum shape is the method of source preparation. This was done by microdispensing an aqueous solution of ammonium pertechnetate ( $\text{NH}_4^{99}\text{TcO}_4$ ) in  $0.1 \text{ mol L}^{-1}$  ammonia ( $\text{NH}_3$ ) with an activity of  $A(^{99}\text{Tc}) \approx 5 \text{ Bq}$  onto a solid gold absorber substrate with a thickness of  $90 \mu\text{m}$ . The source is enclosed by diffusion welding a second  $90 \mu\text{m}$  gold layer to the first one, with more details of the source preparation process being described in [34]. The absorber is attached to one pixel of the MMC detector with Stycast 1266 epoxy and the second pixel is equipped with a second absorber prepared in the same way, but without any radioactive source material. The choice of photon calibration source also has an impact on the spectrum shape.  $^{57}\text{Co}$  with an activity of about  $37 \text{ kBq}$  was used for the measurement at PTB as its spectrum with several peaks is easily distinguishable from the  $\beta$  spectrum shape of  $^{99}\text{Tc}$ . A 1.5-mm-thick lead collimator with two  $250 \mu\text{m}$  apertures blocks the calibration photons outside of the two detector pixels. The apertures are blocked between detector and collimator with an approximately 1-mm-thick aluminium sheet to reduce secondary radiation from the lead without significantly impacting the high-energy photon flux from the  $^{57}\text{Co}$  source.

The detector was operated in a pulse-tube precooled  $^{3/4}\text{He}$  dilution refrigerator (Bluefors LD250) temperature stabilized to  $T = 14.5 \text{ mK}$  on a detector module described in [10]. The used MMC (size M) is an update to the one described in the same publication, with some layout changes improving on experimental shortcomings observed with the first design (e.g., the two on-chip heat baths were linked in the new design to improve thermalization), without changing the core properties of the detector. The setup is completed with a PTB SQUID (model C6X114W) for MMC readout, a Magnicon XXF-1 SQUID electronics, a Stanford Research Systems SR560 low-noise voltage pre-amplifier and band-pass filter, and a 16-Bit waveform digitizer, that was set to save the full

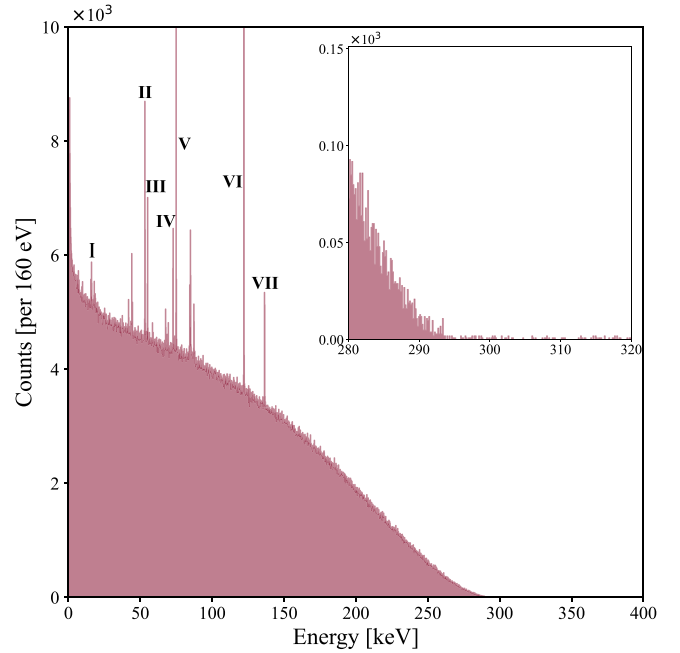


FIG. 4. Measured and calibrated PTB MMC spectrum of  $^{99}\text{Tc}$  with  $^{57}\text{Co}$  calibration source peaks of which seven were used for calibration: Escape lines at 16.13 keV, 53.26 keV, 55.07 keV (denoted I, II, III); Au photons escape the absorber, generated by fluorescent Pb lines and  $\gamma$  rays from the  $^{57}\text{Co}$  source); 72.81 keV, 74.97 keV (denoted IV, V: Pb fluorescence from the setup material); and  $\gamma$  rays at 122.06 keV, 136.47 keV (denoted VI, VII directly from the  $^{57}\text{Co}$  source). Please see Table III for further details. Inset: Spectrum and background around the maximum  $\beta$  energy.

data stream at  $200 \text{ kS s}^{-1}$  to hard disk for the measurement's duration of about 20 days. The data processing and analysis are performed with a custom software code written in PYTHON [35], which performs the next steps that comprise event triggering, amplitude/energy determination, event classification through pulse-shape discrimination, and gain drift corrections. The analysis yields 5 326 682 counts in the spectrum after cuts. The resulting amplitude distribution is calibrated with several  $^{57}\text{Co}$   $\gamma$  lines, x-ray fluorescence, and x-ray escape lines using a second-order polynomial, returning the spectrum shown in Fig. 4. The calibration error was estimated with the uncertainties from the literature values and the statistical uncertainties of the measured peaks using orthogonal distance regression [29,36–38]. The statistical uncertainty was defined as  $\sigma_{\text{Gauss}}/\sqrt{N_{\text{peak}}}$ , where  $\sigma_{\text{Gauss}}$  denotes the standard deviation of a Gaussian function that was fitted to the peak and  $N_{\text{peak}}$  is the number of counts in the peak. The same procedure was done with the pixel without radioactive source material, yielding a spectrum containing the  $^{57}\text{Co}$  calibration spectrum and any additional background. There, a line spectrum with 132 235 counts was extracted.

## 3. Cross analysis

In both institutes, the analog to digital converter (ADC) signals were directly streamed to hard disk and the data were saved as binary files containing 16-bit integers. Therefore,

TABLE IV. Overview of the cross validation with counts, FWHM, and energy threshold ( $=E_{\text{TH}}$ ) values. Set 1 only considered a subset of the recorded data.

Set	Meas.	Analysis	Counts	FWHM	$E_{\text{TH}}$
1	PTB	LNHB	$3.67 \times 10^6$	63 eV at 136.47 keV	345 eV
2	PTB	PTB	$5.33 \times 10^6$	72 eV at 136.47 keV	750 eV
3	LNHB	LNHB	$7.26 \times 10^6$	150 eV at 302.8 keV	1120 eV
4	LNHB	PTB	$5.66 \times 10^6$	108 eV at 302.8 keV	1250 eV

the raw data of both measurements are compatible with each other. This prompted an exchange of the data and a mutual analysis at both institutes to identify any systematic differences introduced by the data processing code or analysis approach. The data processing and analysis were conducted as usual for local data sets and allowed for the comparison between the four spectra in total resulting from two measurements with two analyses each.

For both data sets, the two separate analyses yield surprisingly different numbers of counts, as can be seen in Table IV. The PTB measurement involuntarily stopped during the campaign and was restarted. This caused inconsistencies in the data and, for the analysis at PTB, successful corrections were implemented. In contrast, the LNHB analysis only used the largest continuous data set, which contained about three-quarters of the total data. The remaining difference, also for the LNHB measurement, is most likely caused by differences in the implementation and the settings for the software trigger, and possibly by cuts for event selection. The trigger threshold should only influence the energy threshold, but other settings, such as trigger hold-off or extending/nonextending dead time, etc., can have an impact over the whole energy range. Specifically, for the LNHB-LNHB (set 3) analysis, a very short event time window was chosen, which allows one to reduce the impact of pile-up, with the trade-off of a slightly diminished energy resolution and higher energy threshold.

It was agreed upon to use the same calibration lines for the energy calibration in the spectra and the corresponding literature values for the  $\gamma$  [39,40] and x-ray [33] energies. These lines were very easy to identify and to fit in the spectrum. The tabulated energies and differences to the measurement data are summarized in Table III.

#### 4. Spectrum corrections

Before the actual shape of the  $^{99}\text{Tc}$   $\beta$  spectrum can be investigated, two corrections need to be applied to the measured data. First, the contributions from the calibration sources and additional background need to be removed. Second, the spectrum needs to be corrected for energy losses of the  $\beta$  electrons, mostly caused by x-ray fluorescence of the absorber material and escaping bremsstrahlung.

The simplest way to account for background is to assume a constant background, with its level being determined from the background above the endpoint of the  $\beta$  spectrum. This approach could, e.g., be sufficient for the data taken at PTB and is used in its analysis at LNHB, since no major background sources or  $\gamma$  lines are expected in the endpoint region of the  $\beta$

spectrum, where background has the strongest impact on the spectrum shape. With this background model, the spectrum shape cannot be evaluated at the position of  $\gamma$  lines, which is not a big drawback because of the narrow linewidths.

For the measurement at LNHB, this approach needs to be extended because several calibration lines are close to and even above the  $\beta$  endpoint region. While the background between lines can reasonably be assumed to be constant, the level becomes slightly higher below each line and the background is described as a series of step functions, with the step height being proportional to the line intensity. With this approach, the background in both analyses can be reasonably well described.

The measurement at PTB also offers a different approach to evaluate the background, which is used in the PTB analysis. The second pixel of the detector is equipped with an absorber without any enclosed radioactive material, which is also illuminated by the calibration source. Therefore, the spectrum of the second pixel should be a very good approximation for the background of the primary pixel. Since the detector performance, e.g., in rise time and energy resolution, is not exactly the same, these need to be adjusted and the amplitude of the measured background spectrum scaled to match the intensity of the primary pixel, before the background is subtracted. Since the primary pixel showed the better energy resolution ( $\Delta E_{\text{FWHM}} = 72$  eV compared to  $\Delta E_{\text{FWHM}} = 92$  eV), the primary spectrum was convolved with a normalized Gaussian with  $\Delta E_{\text{FWHM}} = 28$  eV to match the secondary spectrum and the secondary spectrum was scaled by a factor of 0.73 because of its larger intensity.

To account for energy losses in the absorber, mainly via unstopped photons generated by excitation of Au atoms and bremsstrahlung, an unfolding correction was applied to each spectrum before determining the maximum  $\beta$  energy. The unfolding procedure is based on an algorithm that does not require any *a priori* knowledge of the true  $\beta$  spectrum [29,41]. Its basis is the following discrete unfolding problem:

$$\mathbf{h}_N^{\text{meas}} = \mathbf{R}_{N \times N} \cdot \mathbf{h}_N^{\text{true}}, \quad (3)$$

where  $\mathbf{h}_N^{\text{meas}}$  is the measured histogram spectrum having  $N$  energy bins,  $\mathbf{R}_{N \times N}$  denotes the response matrix of the absorber for the  $N$  energy intervals, and  $\mathbf{h}_N^{\text{true}}$  is the unknown true histogram spectrum. After a measurement, one only obtains a value for the left-hand side of (3) and thus the problem is typically high dimensional and greatly underdetermined. However, an excellent approximation of the response matrix  $\mathbf{R}_{N \times N}^{\text{sim}} \approx \mathbf{R}_{N \times N}$  can be acquired via large-scale Monte Carlo (MC) simulations of the corresponding absorber geometries. Since it can be shown that the approximate matrix is invertible with probability 1 [41], the algorithm provides an approximate solution to Eq. (3),

$$\mathbf{h}_N^{\text{true}} \approx \mathbf{h}_N^{\text{algo}} \stackrel{!}{=} (\mathbf{R}_{N \times N}^{\text{sim}})^{-1} \cdot \mathbf{h}_N^{\text{meas}}. \quad (4)$$

The adopted absorber geometries are, notably, just an approximation since the exact distributions of the activity within the rather complex sources are not precisely known. In addition, the imperfect knowledge of the cross sections (e.g., for bremsstrahlung) contribute to the related uncertainty

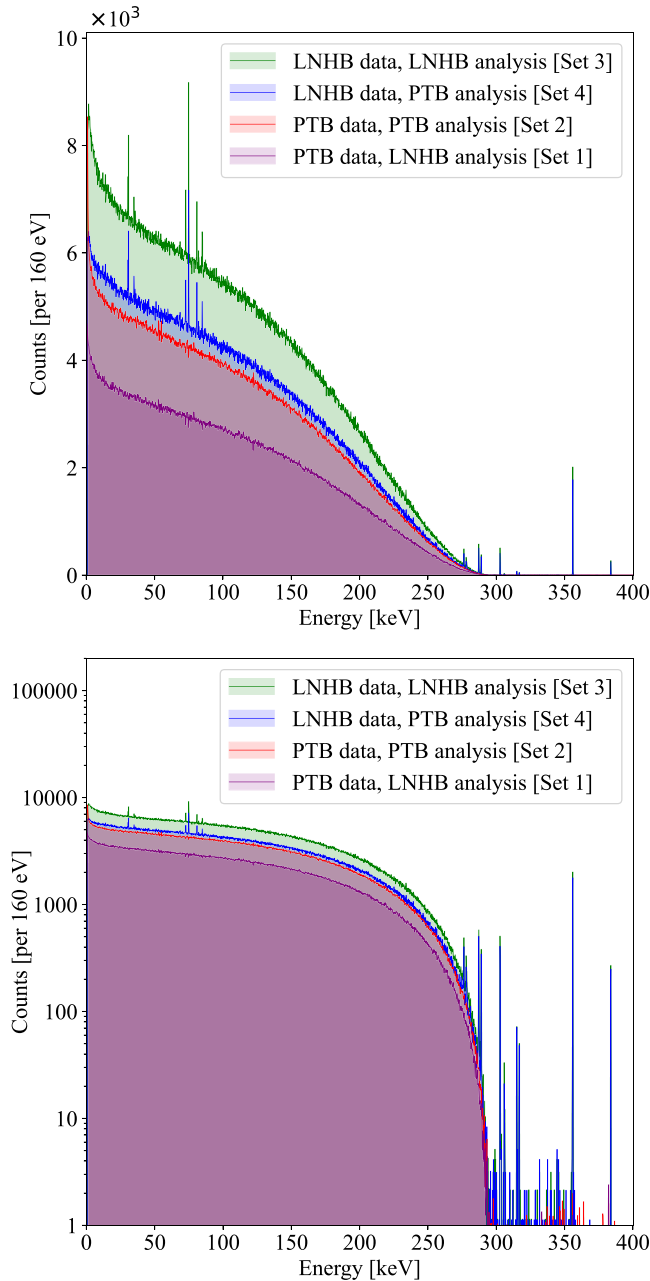


FIG. 5. The  $^{99}\text{Tc}$  spectra measured by MMCs, with their separate analyses in linear scale (top) and logarithmic scale (bottom). Background and energy losses have been corrected as described in the text.

component. The MC simulations were realized with the code `egs_phd` within the EGSNRC software [42] and were performed separately for the PTB and LNHB detector geometries. The resulting four spectra with the background removed and energy loss corrections applied are shown in Fig. 5.

### 5. Intercomparison

After applying the corrections to the spectra as described, all four spectra should, in principle, show the same spectrum shape. Before these can be directly compared, they need to be normalized. We used the total number of events in the

energy range from 150 keV to 250 keV as the normalization factor because there are no  $\gamma$  lines in that range in either measurement. Furthermore, the difference of the normalized counts was divided by the sum of absolute differences. Thus, the resulting normalized residuals sum to unity, i.e., 100%. Normalized residual plots of the various MMC sets (see Table IV) are depicted in Fig. 6. For the same data sets, the analyses yield very small residuals close to the mean and below 5% (proportional contribution to the residual sum) at energies below 1.5 keV. These residuals are due to different  $\chi$ -square and energy cuts, which are set manually. The LNHB data were not background cleaned with experimental data concerning the calibration peaks and these can be seen when compared to the PTB data, showing a very similar pattern for the different analyses.

## B. Silicon detectors

The MMC results were compared to an independent measurement performed with a detection system recently developed at LNHB [43,44]. The system was designed for the measurement of  $\beta$  spectra and is based on two PIPS detectors with thin entrance windows. Such detectors are commonly used to detect charged particles in nuclear and particle physics.

### 1. Experimental setup

The geometry of the overall system is designed such that the PIPS detectors face each other. An ultrathin radioactive source developed specifically for this application [45,46] is placed in their center. The experimental configuration covers more than 98% of the solid angle and minimizes the self-absorption within the source. Consequently, experimental distortions of the spectrum are significantly reduced. Source and detectors are placed in an ultrahigh vacuum chamber, while the detection system is cooled down to 100 K with liquid nitrogen, in order to improve the energy resolution and lower the detection threshold. The detector output is preamplified in the chamber before being shaped and recorded using a LABZY module [47]. A complete description of the detector design, acquisition system, and source fabrication can be found in [48].

### 2. Analysis and corrections

The analysis of the data was performed in C++ using the ROOT software [49]. The system was calibrated with  $^{109}\text{Cd}$  and  $^{207}\text{Bi}$  sources whose emissions cover an energy range from about 22 to 1063 keV, as described in [48]. The energy resolution of the detection system was determined to be 9 keV at 65.52 keV, where an energy peak due to Ag  $K$  shell electrons, which are emitted by internal conversion in  $^{109}\text{Cd}$  decay, is situated. The calibration sources were also used to determine the detection energy threshold, which was estimated to be about 10 keV.

The activity of the  $^{99}\text{Tc}$  source was about 800 Bq in order to limit the dead-time ratio of the acquisition to less than 0.5%. The measurement was performed over five consecutive days. To estimate the contribution of the background to the

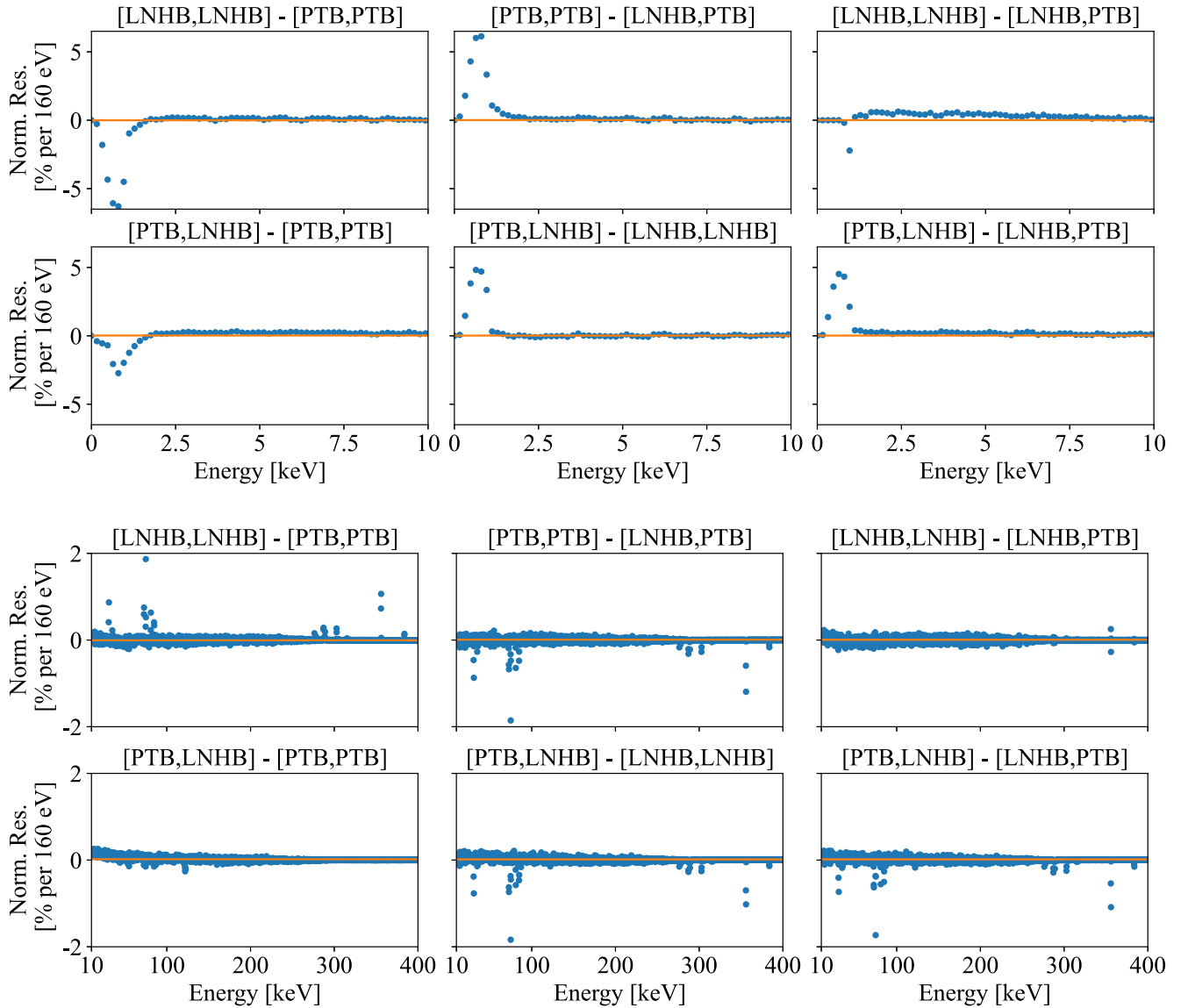


FIG. 6. Analysis comparison for the two MMC measurements of the  $^{99}\text{Tc}$  spectrum (data, analysis): normalized residual point plots (blue) and mean of residuals (orange). Rows 1 and 2 show the low-energy range from 0 to 10 keV and rows 3 and 4 depict the remaining energy range from 10 to 400 keV. Plots are shown for sets 3 and 2 (rows 1 and 3, left), sets 2 and 4 (rows 1 and 3, center), sets 3 and 4 (rows 1 and 3, right), sets 1 and 2 (rows 2 and 4, left), sets 1 and 3 (rows 2 and 4, center), and sets 1 and 4 (rows 2 and 4, right).

spectrum, a ten-day measurement was performed with a source produced with a nonradioactive solution. The background was found to have little effect on the measured spectrum, as 80% of the background events was detected below 15 keV. For the data analysis, the background spectrum was subtracted from the  $^{99}\text{Tc}$  spectrum after normalization of the lifetime ratios of the measurements.

To account for the remaining distortions in the experimental spectrum, mainly due to energy loss in dead layers and escape of particles, an unfolding algorithm was adapted from the principle presented in [41]. Based on detailed PENELOPE [50] Monte Carlo simulations of the source-detector geometry, the algorithm provides a way to reconstruct the response matrix of the detection system. From this knowledge, the experimental spectrum can be unfolded to obtain the

initial energy distribution of the  $\beta$  electrons. More details on the algorithm and the simulation can be found in [48]. The response function of the detector is considered to be under good control from 850 keV down to at least 25 keV. This is evidenced by the good agreement between the analyzed data from several measured sources and the simulation of the detection system.

### 3. Comparison

The corrected spectrum obtained from the PIPS measurement is compared in Fig. 7 to the two MMC measurements. The three spectra show an excellent agreement from the minimum reconstructed energy of the PIPS system up to the endpoint of the spectra. The PIPS measurement is



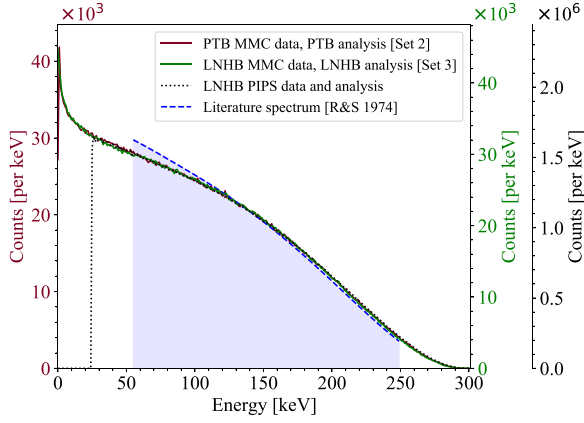


FIG. 7. Comparison of the measured PTB MMC, LNHB MMC, and PIPS spectra after removing the background, in red, green, and black, respectively. Please note the corresponding coloring of the first, second, and third y axis. While the count statistics of the PIPS measurement is approximately 50 times larger than those of the MMCs, its energy resolution is two orders of magnitude smaller (9 keV vs  $\lesssim 90$  eV at 65.52 keV). Shown in blue is the recommended literature spectrum of  $^{99}\text{Tc}$  [15], which was plotted over the experimental measurement interval (55 to 250 keV) using the reported shape factors. Notably, the literature spectrum shape diverges below 100 keV.

independent of the MMC measurements, both in terms of detection method and source preparation, and the consistency between the three spectra underlines the reliability of the  $\beta$  spectra presented in this article. Compared to the recommended  $\beta$  spectrum of  $^{99}\text{Tc}$  in the literature [15], which was reported by Reich and Schüpferling in 1974, there is rather good agreement above 100 keV, but divergence with a clear trend at lower energies. Very likely, the divergence is due to experimental issues in the absorber geometry of [15]. The solid angle was realistically less than  $4\pi$  and, to the best of our knowledge, the resulting energy losses were not corrected, e.g., using an unfolding procedure.

### III. COMBINED ANALYSIS

The results of Sec. III A, concerning the maximum  $\beta$  energy, were carried out at the PTB with theory insight from the LNHB, and the spectrum-shape method calculations of Sec. III B were done at the LNHB.

#### A. $^{99}\text{Tc}$ $Q$ -value

For the determination of the maximum  $\beta$  energy  $E_{\max}$  of  $^{99}\text{Tc}$ , the methodology described in a previous article [51] was adopted to allow for an energy-dependent shape-factor function  $C(W)$ . When neglecting the antineutrino mass, the  $\beta$  spectrum is described by

$$N(W)dW = \frac{G_{\beta}^2}{2\pi^3} F(Z, W) pW (W_0 - W)^2 dW \times X(W) C(W) r(Z, W), \quad (5)$$

where  $N(W)$  corresponds to the measured data,  $F(Z, W)$  is the Fermi function with  $Z$  the daughter atomic number,  $p = (W^2 - 1)^{1/2}$ ,  $W_0 = 1 + E_{\max}/m_e$ , where  $m_e$  is the electron rest mass, and  $W = 1 + E/m_e$ . The constant  $G_{\beta}^2$  is the squared product of the weak interaction coupling constant  $g$  and the cosine of the Cabibbo angle,  $\cos \Theta_C$ , and  $X(W)$  stands for the correction of the atomic screening and exchange effects. The atomic overlap correction is given by

$$r(Z, W) = 1 - \frac{1}{W_0 - W} \frac{\partial^2}{\partial Z^2} B(G). \quad (6)$$

For  $^{99}\text{Tc}$ , the constant  $B'' = \frac{\partial^2}{\partial Z^2} B(G)$  and its uncertainty was calculated to be  $B'' = 0.211(11)$  keV when using parametrizations from the literature [52,53].

The shape-factor function of the second forbidden nonunique  $\beta$  transition of  $^{99}\text{Tc}$  is often parameterized as first forbidden unique using

$$C(W) = q^2 + \lambda p^2 = (W_0 - W)^2 + \lambda(W^2 - 1), \quad (7)$$

with  $\lambda$  being a constant parameter (see, e.g., [15]). Hence, Eq. (5) can be rearranged to get

$$\sqrt{\frac{N(W)}{pWF(Z, W)X(W)}} = K \{ [(W_0 - W)^2 - B''(W_0 - W)] \times [(W_0 - W)^2 + \lambda(W^2 - 1)]^{1/2}, \quad (8)$$

which is then used for the fit procedures. In contrast to standard Kurie fits [54], the fit function [right side of Eq. (8)] is not linear, but the three parameters ( $K$ ,  $W_0$ , and  $\lambda$ ) can be directly determined in a single fit process.

The analysis was carried out with all four MMC data sets (two measurements  $\times$  two analyses). To this end, spectra with the background removed and corrected for bremsstrahlung losses and with a bin width of 160 eV were used as a starting point. If the used background model left the photon peaks of the external sources ( $^{57}\text{Co}$  and  $^{133}\text{Ba}$ , respectively) in place, these were removed. The uncertainty assigned to the background was conservatively estimated. To this end, the analysis was repeated without any background subtraction. The difference to the previous result with background subtraction was then used to evaluate the corresponding uncertainty component assuming a rectangular distribution. It should be noted that the influence of background to the determined maximum  $\beta$  energy also depends on the energy range that is considered for the fits.

For all cases (sets 1–4), the spectrum unfolding shifted the maximum energy by approximately +200 eV. The impact on the spectrum shape, however, is very subtle as the energy losses of the absorbers were very small ( $< 1\%$ ) in these experiments. If the energy losses are larger, the unfolding affects the spectrum shape more significantly [29,41,44].

Results of the fit procedure are shown in Table V and an uncertainty budget is shown in Table VI. The fit ranges were chosen in order to study several potential effects such as the interplay between shape-factor function and  $E_{\max}$ . The third range (125 to 293.5 keV) was included to demonstrate that consistent results are obtained, even if a high upper limit close

TABLE V. Results for the maximum  $\beta$  energy  $E_{\max}$  obtained using spectra from the two analysis codes and two measurements. The results correspond to mean values that were obtained from three individual results using different energy ranges for the fits (70 to 290 keV, 140 to 290 keV, and 125 to 293.5 keV, respectively). In all cases, the measurement uncertainties were taken into account (weighted fits), the background was subtracted, spectrum unfolding was taken into account, and the shape-factor function  $C(W) = q^2 + \lambda p^2$  was assumed. The currently recommended  $E_{\max}$  values in the literature are 293.8 keV [15] and 297.5(9) keV [17], respectively.

Set	Measurement	Analysis	$E_{\max}$ (keV)	$\lambda$
1	PTB	LNHB	295.809	0.615
2	PTB	PTB	295.786	0.652
3	LNHB	LNHB	295.845	0.651
4	LNHB	PTB	295.862	0.659

to the endpoint energy is chosen. This may be different for historical studies, which can suffer from low-energy resolution and the related resolution distortion effect.

The evaluation of further uncertainty components was carried out in a similar manner as described in Ref. [51]. For the uncertainty analysis, fit ranges were varied and unweighted fits were compared with fits that take statistical uncertainties into account. In order to evaluate a model uncertainty, the analyses were repeated, ignoring the correction for screening and the atomic exchange effect and by using a modified shape-factor function  $C(W) = 1 + aW + b/W + cW^2$ . In this case, the mean result agrees to within 74 eV. However, a somewhat larger spread of results for the maximum energy is observed when using this shape-factor parametrization, which might be due to the larger number of adjustable parameters. The uncertainty budgets for both measurements are listed in Table VI. The individual results  $E_{\max} = 295.798(156)$  keV for the PTB measurement and  $E_{\max} = 295.854(199)$  keV for the LNHB measurement are used to calculate a weighted mean as our final result:

$$E_{\max} = 295.82(16) \text{ keV.} \quad (9)$$

The uncertainty of the final result corresponds to the uncertainty of the PTB result and is more conservative than the inner (123 eV) and outer (3 eV) uncertainties of the weighted mean and we can exclude an underestimation of the uncertainty due to correlations. The analysis described above also provides information on the parameter  $\lambda$ . However, the analysis is dedicated to the determination of the maximum energy and it does not consider the low-energy part of the  $\beta$  spectrum. Thus, the stated  $\lambda$  values are not necessarily suited to describe the spectrum shape in a wide energy range.

## B. The spectrum-shape method

In usual descriptions of nuclear  $\beta$  decay, the Hamiltonian density is expressed in terms of lepton and hadron currents. Assuming a pure ( $V - A$ ) weak interaction, transition matrix elements are of the vector type, associated to the vector coupling constant  $g_V$ , or of axial-vector type, associated to the axial-vector coupling constant  $g_A$ . The conserved vector

current (CVC) hypothesis derives from the gauge invariance of the weak interaction and leads to  $g_V = 1$ . According to the partially conserved axial-vector current (PCAC) hypothesis, one can adopt the free-nucleon value  $g_A^{\text{free}} = 1.2754(13)$  [55].

An ideal description of the nuclear structure would allow the use of these values in  $\beta$  decay calculations. However,  $g_V$  and  $g_A$  can be renormalized because of the imperfections of the nuclear model that is employed. This has been well known for a long time from the study of partial half lives (see, e.g., the review of Suhonen [56]). Effective values of the coupling constants then help to compensate for some approximations such as nonexistent or partial core excitations, or simplified many-nucleon correlations. However, one has to note that this renormalization could not have a physical meaning, but is more an artifact due to the nuclear model. The last decade has seen important progress thanks to the development of effective field theories. It was recently demonstrated that for allowed Gamow-Teller transitions, the 0.8 quenching factor on  $g_A$  obtained with the nuclear shell model becomes unnecessary to reproduce the decay rates when advanced *ab initio* computations, including two-body currents, are employed [57]. In the present analysis, we have considered nuclear structure information from the nuclear shell model only.

Recent theoretical studies suggested that  $g_A^{\text{eff}}$  can also have a significant influence on the spectrum shape of forbidden nonunique transitions [58,59]. Indeed, the calculation of forbidden nonunique transitions involves nonrelativistic axial-vector matrix elements that are associated to the  $g_A$  constant. In particular,  $^{99}\text{Tc}$  decay was predicted to be very sensitive to  $g_A^{\text{eff}}$ , making this spectrum a good candidate for a precise determination [8]. This approach, called the spectrum-shape method and introduced in [58], was applied in the present work. The analysis was carried out on the spectrum measured and analyzed at PTB, chosen for its lower background correction. Because full computation of the  $\beta$  spectrum is time consuming, the energy binning was increased to 1 keV. The maximum energy used as the input parameter was from this work, as described above.

In Suhonen's review [56], the effective coupling constant was mostly predicted to be quenched, and a formula is given to estimate the part of the quenching factor related to nuclear medium effects from a quenching factor in infinite nuclear matter. Applied to  $^{99}\text{Tc}$  decay, we obtained  $g_A^{\text{inf}} = 1.120$ . In addition, a conflicting result was stressed for the forbidden nonunique transitions. In first forbidden transitions, the single-particle estimates of the effective coupling constants are found to be  $g_V^{\text{eff}} \approx 0.3\text{--}0.7$  and  $g_A^{\text{eff}} \approx 0.46\text{--}0.56$ . For higher forbidden transitions, only two fourth forbidden nonunique transitions were studied, namely,  $^{113}\text{Cd}$  and  $^{115}\text{In}$  decays, and the best adjustment with the existing measurements led to an unquenched value of  $g_V$  and  $g_A^{\text{eff}} \approx 0.9$ . The high precision measurement of the  $^{99}\text{Tc}$  spectrum from this work brings a new, important constraint.

### 1. $\beta$ spectrum modeling

The method to calculate the  $\beta$  spectrum has already been described in [51,60] and follows the formalism of Behrens and Bühring [61]. The theoretical spectrum is described by

TABLE VI. Uncertainty budgets for the maximum  $\beta$  energy  $E_{\max}$  for the two measurements. All uncertainties are stated as standard uncertainties ( $k = 1$ ).

Uncertainty component	LNHB meas.		PTB meas.		Comment
	$u$ (eV)	Relative uncertainty	$u$ (eV)	Relative uncertainty	
Energy calibration	45	0.015%	50	0.017%	Several well-known peaks used for the calibration, high reproducibility, different calibration sources in the two measurements ( $^{57}\text{Co}$ and $^{133}\text{Ba}$ )
Resolution distortion effect, finite energy resolution	10	0.003%	10	0.003%	Bins at high energies avoided; these effects are further described in Kossert <i>et al.</i> [51].
Background	141	0.048%	69	0.023%	Background taken into account
Fit method	93	0.031%	89	0.030%	Variation of energy range; weighted vs unweighted fit, rebinning
Theoretical model	75	0.025%	75	0.025%	Analysis with other shape-factor parametrization, difference with/without screening and exchange
Spectrum unfolding	57	0.019%	57	0.019%	Dependence on cross sections (e.g., bremsstrahlung) and geometry
Analysis software/pile-up	10	0.003%	10	0.003%	Deviation when using input spectra obtained from the two analysis codes
Combined	199	0.067%	156	0.053%	

Eq. (5) on which the radiative corrections given in [52] are also applied. Two terms, however, are calculated differently: the atomic exchange correction and the shape factor.

The modeling of the atomic exchange effect was developed decades ago for the allowed transitions [62], and was recently extended to the forbidden unique transitions [63]. Applying Eq. (3) in [63] allowed us to calculate the exchange effect specifically for the second forbidden nonunique transition in  $^{99}\text{Tc}$  decay. To this purpose, it is necessary to introduce nuclear structure information, which is also needed for the shape factor and which we detail now.

The shape factor  $C(W)$  in Eqs. (5) and (7) is experimental, i.e., its global energy dependency is based on some theoretical arguments, but is adjusted on the measured spectrum. To extract the coupling constants,  $C(W)$  must be purely theoretical. The shape factor is a convolution of the nuclear structure and the lepton dynamics and is usually expanded in different multipoles of both the nuclear and lepton currents,

$$C(W) = \sum_{K, k_e, k_\nu} \lambda_{k_e} \left[ M_K^2(k_e, k_\nu) + m_K^2(k_e, k_\nu) - \frac{2\mu_{k_e} \gamma_{k_e}}{k_e W} M_K(k_e, k_\nu) m_K(k_e, k_\nu) \right]. \quad (10)$$

Quantities labeled by the lepton quantum numbers  $k_e$  and  $k_\nu$  depend on the relativistic wave functions, and  $K$  is the principal nuclear multipole order. The lepton current was simplified by Behrens and Bühring in order to decouple the calculation of lepton and nuclear matrix elements. The procedure consists in expanding the lepton radial wave function in powers<sup>1</sup> of

$(m_e R)$ ,  $(WR)$ , and  $(\alpha Z)$  and is here referred to as the truncated lepton current. In the case of the second forbidden nonunique  $^{99}\text{Tc}$  decay, we followed Behrens' and Bühring's recommendation, keeping only the dominant terms [61]. It is noteworthy that in [56], the authors also considered next-to-leading-order terms as described in [64]. This procedure is possible only with a simplified Coulomb potential. As in our previous study of  $^{151}\text{Sm}$  decay [51], we also considered a full numerical lepton current based on lepton wave functions determined by solving the Dirac equation with a Coulomb potential that includes atomic screening. All the terms of the lepton wave-function expansion are therefore virtually accounted for.

For calculating the shape factor, an input from a realistic nuclear structure model is required. The NUSHELLX code [65] was used in this work to determine the list of nucleon-nucleon transitions that contribute to the  $^{99}\text{Tc}$  decay. These single-particle transitions are weighted by their corresponding one-body transition densities (OBTDs). Following [8], we first considered the effective interaction from Gloeckner [66] with the  $GL$  valence space spanning the proton orbitals  $2p_{1/2}$  and  $1g_{9/2}$ , and the neutron orbitals  $3s_{1/2}$  and  $2d_{5/2}$ . With such a description, the  $^{99}\text{Tc}$  decay is driven by a single nucleon-nucleon transition, from a neutron in  $2d_{5/2}$  to a proton in  $1g_{9/2}$ . Next, the effective interaction from Mach [67] with the wider  $GLEKPN$  valence space was considered. This valence space spans the proton orbitals  $1f_{7/2}$ ,  $1f_{5/2}$ ,  $2p_{3/2}$ ,  $2p_{1/2}$ , and  $1g_{9/2}$ , and the neutron orbitals  $1g_{9/2}$ ,  $1g_{7/2}$ ,  $2d_{5/2}$ ,  $2d_{3/2}$ , and  $3s_{1/2}$ . To limit the computational burden, the  $1f_{7/2}$  proton and the  $1g_{9/2}$  neutron orbitals were constrained to be full, and four protons were blocked in the  $1f_{5/2}$  orbital. As a result, the  $^{99}\text{Tc}$  decay is still dominantly driven by the same single-particle transition, but a small admixture of a transition from a neutron in  $1g_{7/2}$  to a proton in  $1g_{9/2}$  appears (see Table VII for the dominant multipole order  $K = 2$ ). Finally, we also considered the  $jj45pnb$  interaction [68] with the valence space spanning

<sup>1</sup> $R$  is the daughter nucleus radius and  $\alpha$  is the fine-structure constant.

TABLE VII. One-body transition densities (OBTDs) of the dominant multipole order ( $K = 2$ ), as given by NUSHELLX. Coulomb displacement energies for each nucleon-nucleon transition are also given (MeV).

One-particle transition	OBTDs	$\Delta E_C^{(3)}$	$\overline{\Delta E_C^{(4)}}$	$\overline{\Delta E_C^{(4)}}$
$1g_{7/2} \rightarrow 1g_{9/2}$	0.00994	11.696	12.051	12.045
$2d_{5/2} \rightarrow 1g_{9/2}$	0.47752	10.560	10.536	10.537

$1f_{5/2}$ ,  $2p_{3/2}$ ,  $2p_{1/2}$ , and  $1g_{9/2}$  for protons, and  $1g_{7/2}$ ,  $2d_{5/2}$ ,  $2d_{3/2}$ ,  $3s_{1/2}$ , and  $1h_{11/2}$  for neutrons. The only constraint applied was a minimum of four protons in the  $1f_{5/2}$  orbital. OBTDs are quite close to those obtained with *GLEKPN*, but noticeably of opposite sign for the dominant multipole order: 0.011 07 for  $1g_{7/2} \rightarrow 1g_{9/2}$  and  $-0.439$  85 for  $2d_{5/2} \rightarrow 1g_{9/2}$ .

The transition probability of a forbidden nonunique decay first depends on a relativistic vector matrix element. While a nonrelativistic matrix element couples the large components of the nucleon wave functions, a relativistic matrix element couples their small and large components together. However, most of the nuclear models, as NUSHELLX, are nonrelativistic. An accurate estimate of this relativistic vector matrix element can be obtained from a nonrelativistic vector matrix element employing the CVC hypothesis (see, e.g.,  $^{36}\text{Cl}$  decay in [69]). In  $^{99}\text{Tc}$  decay, the relationship is

$${}^V F_{221} \simeq -\frac{R}{\sqrt{10}} [W_0 - (m_n - m_p) + \Delta E_C] {}^V F_{220}, \quad (11)$$

with  $m_n$  and  $m_p$  the neutron and proton rest masses and  $\Delta E_C$  the Coulomb displacement energy. The small  $Q$ -value of  $^{99}\text{Tc}$  decay makes a critical good estimate of  $\Delta E_C$  because  $[W_0 - (m_n - m_p)] = -0.487$  MeV only.

The Coulomb displacement energy can be estimated from different methods. Usually, a uniformly charged sphere is considered and the expression only depends on the daughter nucleus through its atomic number and its nuclear radius,

$$\Delta E_C^{(1)} = \frac{6}{5} \frac{\alpha Z_f}{R_f} = 13.476 \text{ MeV}. \quad (12)$$

A similar expression can be established that depends on both the parent and daughter atomic numbers and their nuclear radii,

$$\Delta E_C^{(2)} = \frac{3}{5} \frac{\alpha}{R_f} Z_f (Z_f - 1) - \frac{3}{5} \frac{\alpha}{R_i} Z_i (Z_i - 1) = 12.814 \text{ MeV}. \quad (13)$$

However,  $\Delta E_C$  is known to possibly be sensitive to the mismatch between the initial and final nucleon wave functions [70]. Behrens and Bühring approximated the single-particle potential difference by the average of the Coulomb potential, keeping only the leading order of the lepton current [61],

$$\Delta E_C^{(3)} = \frac{\int_0^\infty g_f V(r) g_i (r/R)^K r^2 dr}{\int_0^\infty g_f g_i (r/R)^K r^2 dr}, \quad (14)$$

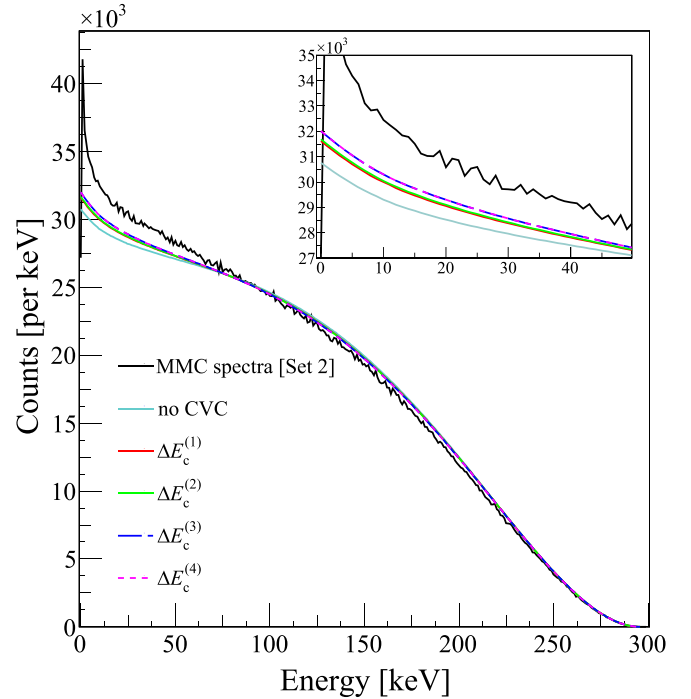


FIG. 8. Comparison of the measured  $^{99}\text{Tc}$  spectrum with different theoretical curves. CVC is either ignored or included for different estimates of the Coulomb displacement energy  $\Delta E_C$ . Inset: The low-energy part of the spectrum.

where  $g_i$  and  $g_f$  are the radial large components of the initial and final nucleon wave functions, respectively. This Coulomb displacement energy  $\Delta E_C^{(3)}$  is thus different for each nucleon-nucleon transition, but is still independent of the  $\beta$ -particle energy. Finally, one can also introduce a dependency on the  $\beta$ -particle energy by considering the complete lepton current, instead of the leading order  $(r/R)^K$ . The corresponding Coulomb displacement energy is denoted  $\Delta E_C^{(4)}$  and also depends on the lepton quantum numbers  $k_e$  and  $k_\nu$ . This latter method is, in principle, the most accurate. In Table VII, we give  $\Delta E_C^{(3)}$  and the average value of  $\Delta E_C^{(4)}$  for the dominant nucleon-nucleon transitions. In practice, the dependency of  $\Delta E_C^{(4)}$  in the  $\beta$ -particle energy was found to be less than 1 keV over the entire energy range of the spectrum.

In Fig. 8, we present the spectrum calculated without the CVC hypothesis, and the spectra considering CVC for the different  $\Delta E_C$  estimates. The free-neutron value of  $g_A$  was assumed. CVC has an influence but does not lead to a change of the spectrum shape as spectacular as in  $^{36}\text{Cl}$  decay [69]. The spectrum mostly exhibits a dependency at low energy and the spectra with  $\Delta E_C^{(3)}$  and  $\Delta E_C^{(4)}$  are hardly distinguished. In addition, we tried to adjust  $\Delta E_C$  in order to be as close as possible to the measured spectrum. The best value was found to be  $\Delta E_C = 3.57$  MeV with a poor reduced- $\chi^2$  of 5.018, and a nonlinear tendency was found in the residuals. Most of all, it is clear that the adjusted Coulomb displacement energy is not realistic.

This result supports an adjustment of the coupling constants to retrieve the measured spectrum. We chose as a reference for the fitting procedure the spectrum calculated

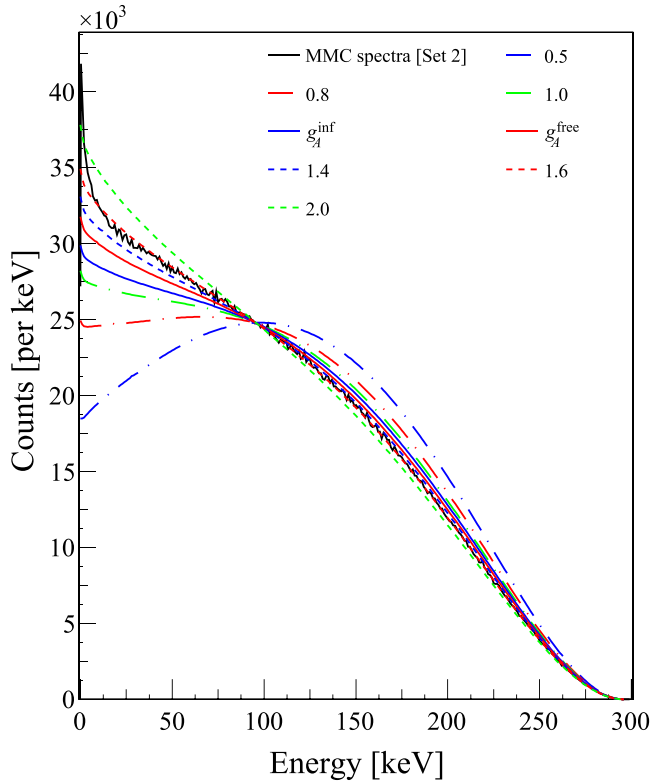


FIG. 9. Influence of the effective  $g_A$  value on the theoretical  $\beta$  spectrum of  $^{99}\text{Tc}$  decay, compared to the high precision measurement from this work.

considering a full numerical treatment of the lepton current, the OBTDs from the *GLEKPN* valence space with Mach interaction, and the CVC hypothesis with the  $\Delta E_C^{(4)}$  Coulomb displacement energy. All other possibilities were used to estimate uncertainties.

## 2. Effective coupling constants

Based on the modeling described above, we followed the approach in [8,71] varying only  $g_A$ . One should underline that the CVC hypothesis was not used in [8], but was in [71]. As illustrated in Fig. 9, we indeed observed a high sensitivity of the spectrum shape on the effective  $g_A$  value. Quick inspection clearly shows that a  $g_A^{\text{eff}}$  value between 1.4 and 1.6 could give good agreement with the measured spectrum from this work. The fit procedure simply consisted in redoing the calculations for different  $g_A^{\text{eff}}$  values until finding the minimum reduced- $\chi^2$ . A reasonable energy range of 20 to 275 keV was considered to determine the central value in order not to be influenced by the first and the last 20 keV of the spectrum, where distortions can be significant. The reduced- $\chi^2$  distribution is very close to a quadratic shape. The best adjusted value is  $g_A^{\text{eff}} = 1.526$  with reduced- $\chi^2 = 1.010$ .

The final spectrum is compared to the high precision measurement from this work in Fig. 10. The agreement is excellent down to 6 keV. The distribution of the residuals does not show any energy dependency and follows a narrow Gaussian distribution, perfectly centered on zero. It is noteworthy that

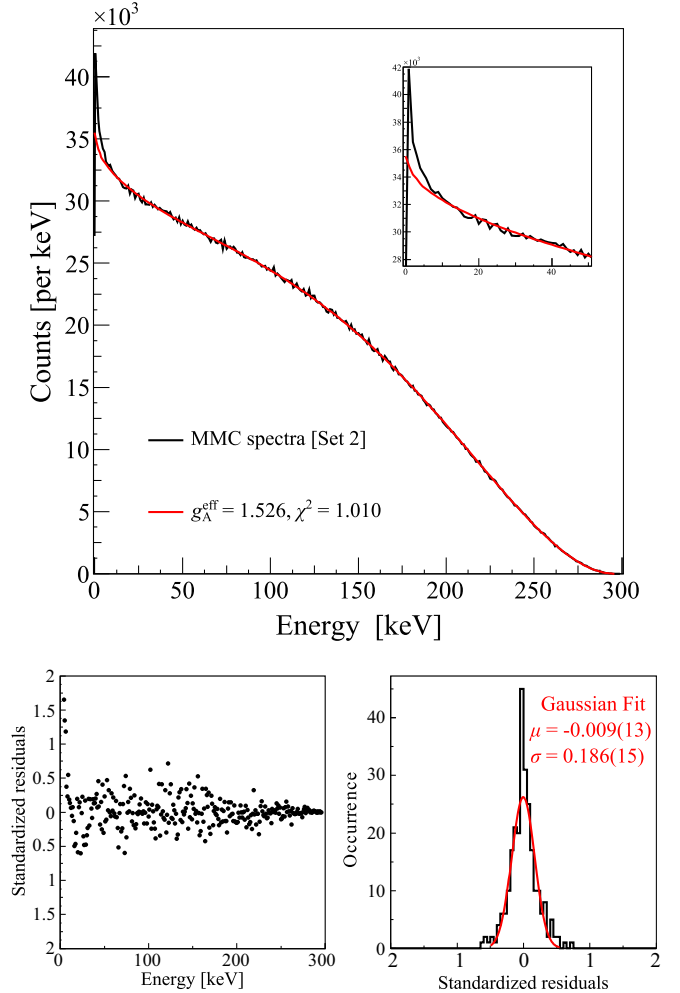


FIG. 10. Comparison of the measured  $^{99}\text{Tc}$  spectrum with the theoretical curve with the best adjusted  $g_A^{\text{eff}}$  value. Inset: The low-energy part of the spectrum and the distributions of the residuals.

such agreement would not have been possible with an erroneous endpoint energy, which validates the extracted  $Q$ -value previously determined. Below 6 keV, the atomic exchange correction does not seem to be sufficiently high to account for the distortion observed in the measured spectrum. We found the same discrepancy in the recent study of  $^{151}\text{Sm}$  decay [51]. A possible explanation could be an inaccurate modeling of the atomic wave functions, as recently pointed out in [72]. These authors provide an analytical fit of their correction, but only for allowed transitions. We applied it only to the Fermi function, which should give the main contribution. The very low-energy part of the spectrum is quite comparable and does not resolve the discrepancy with the measured spectrum. The best adjusted value was found to be  $g_A^{\text{eff}} = 1.520$  with reduced- $\chi^2 = 1.018$ , and was used to estimate an uncertainty component, as explained below.

The uncertainty budget is detailed in Table VIII. Several components were studied and estimated with the minimum-maximum method. Different probability distributions were considered depending on the uncertainty component, with the objective of being realistic and conservative.

TABLE VIII. Uncertainty budget for the  $g_A^{\text{eff}}$  value extracted from the  $^{99}\text{Tc}$   $\beta$  spectrum measured in this work. All uncertainties are stated as standard uncertainties ( $k = 1$ ).

Uncertainty component	Value in $10^{-2}$	Relative uncertainty	Comment
Fit method	7.45	4.88%	Estimate at $\chi^2 \pm 1$ ; includes bin statistics component
Fit range	0.61	0.40%	Largest deviation observed with extreme energy ranges
Maximum energy	0.38	0.25%	$Q$ -value and uncertainty from this work
Nuclear model	2.94	1.93%	Deviation with $jj45pnb$ interaction
Lepton current	1.27	0.83%	Deviation with simplified lepton current and $\Delta E_C^{(3)}$
Coulomb displacement energy	4.25	2.78%	Largest deviation observed with $\Delta E_C^{(1)}$
Atomic exchange	0.29	0.19%	Deviation with correction from [72]
Radiative corrections	0.33	0.21%	Conservative estimate, with or without including them
Combined	9.19	6.02%	$\ell^2$ -norm, i.e., the square root of the quadratic sum

The main contribution comes from the fit method, which also includes the spectrum statistics. The quadratic shape of the reduced- $\chi^2$  distribution allows one to estimate the fit method uncertainty from the  $g_A^{\text{eff}}$  values at reduced- $\chi^2 + 1$ . The chosen energy range for the fitting procedure also has an influence. Two extreme cases were considered, namely, 0 to 296 keV and 100 to 200 keV. The largest deviation was used with a triangular probability distribution. The maximum energy of the spectrum determined in this work was used for the calculation and its uncertainty was propagated with calculations at  $\pm 1\sigma$  considering a rectangular probability distribution.

For the other components, spectrum calculations were performed with different hypotheses,  $g_A^{\text{eff}}$  was extracted, and the largest deviation from  $g_A^{\text{eff}} = 1.526$  was considered with a triangular probability distribution. Uncertainty due to the nuclear model was estimated from the largest obtained deviation, considering either the  $GL$  model space with Gloeckner interaction [66] or the  $jj45pnb$  interaction [68]. The usual simplified lepton current was employed to assess an uncertainty due to lepton current treatment. The different methods for determining the Coulomb displacement energy were tested and the maximum deviation was found with  $\Delta E_C^{(1)}$ . The  $g_A^{\text{eff}}$  value determined with the atomic exchange correction from [72] was considered to estimate an uncertainty due to this correction.

Finally, we considered an uncertainty component due to the radiative corrections. The latter include the emission of real soft photons from the internal bremsstrahlung process. This part of the correction on the  $\beta$  spectrum assumes that these photons are lost and thus not detected. However, there is no doubt that they are partially reabsorbed by the detection system, especially the low-energy photons. A conservative estimate was obtained by simply ignoring the radiative corrections in the spectrum calculation. It is more than an extreme case of possible photon reabsorption because additional corrections that do not come from internal bremsstrahlung are also ignored.

The total combined uncertainty is given in Table VIII. The main component comes from the statistics of the measurement. The value of the effective axial-vector coupling constant

extracted from  $^{99}\text{Tc}$  spectrum is eventually

$$g_A^{\text{eff}} = 1.526(92). \quad (15)$$

It can be surprising that our  $g_A$  value is not quenched but enhanced, far from Suhonen's review value of  $g_A^{\text{eff}} \approx 0.9$ . However, our calculated half life obtained from spectrum integration is  $29.98(85) \times 10^3 a$ , one order of magnitude lower than the evaluated half life  $211.5(11) \times 10^3 a$  [11]. We can very accurately describe the global  $^{99}\text{Tc}$  decay, i.e., both the spectrum shape and the half life, by simply renormalizing the coupling constants with the ratio of these two half lives. We then determined

$$g_V^{\text{eff}} = 0.376(5) \quad \text{and} \quad g_A^{\text{eff}} = 0.574(36). \quad (16)$$

The coupling constants are thus quenched, with values that are noticeably consistent with Suhonen's review values for the first forbidden nonunique transitions. Our result thus seems to solve the inconsistency highlighted by Suhonen in [56].

Considering the full energy range, we determined the average energy of the  $\beta$  spectrum from our calculation,

$$\bar{E}_\beta = 98.51(23) \text{ keV}, \quad (17)$$

and the corresponding  $\log f$  value,

$$\log f = -0.47660(22). \quad (18)$$

With the partial half life from [11], we obtained

$$\log ft = 12.3478(23) \quad (19)$$

for the ground-state to ground-state transition in  $^{99}\text{Tc}$  decay.

Notably, the experimental shape factor from [15] leads to  $\bar{E}_\beta = 95.91(5) \text{ keV}$ ,  $\log f = -0.8785(11)$ , and  $\log ft = 11.9458(25)$ , using the  $Q$ -value from this work.

#### IV. CONCLUSION

In the work described here, it is once again demonstrated that MMC measurements are excellently suited for determining both the shape and the maximum energy of  $\beta$  spectra with  $Q_\beta$ -values below 1 MeV. The measurements are characterized not only by the high linearity and high-energy resolution, but also by the fact that very low detection thresholds can

be reached. The good agreement of two almost independent measurements also in the cross analysis of the data increases confidence in the obtained  $\beta$  spectra. Since the background is the major uncertainty contribution of the obtained maximum  $\beta$  energy, as shown in Table VI, we conclude that experimental design and optimized calibration sources are crucial to improve upon such measurements using MMCs.

High-quality PIPS detector measurements confirm the shape of the spectrum above 25 keV. We do not make a detailed comparison with previous determinations of the shape of the  $\beta$  spectrum, but point out that parametrizations of the  $\beta$  spectrum found in the literature must now be considered obsolete. It should be noted that all previous measurements of the  $^{99}\text{Tc}$   $\beta$  spectrum had significantly higher-energy thresholds, so that a significant part of the spectrum at low energies had to be considered as being unknown. Combining our measurements with detailed theoretical calculations based on the nuclear shell model, we extracted new decay data of interest:  $Q_\beta = 295.82(16)$  keV,  $\bar{E}_\beta = 98.51(23)$  keV,  $\log f = -0.47660(22)$ , and  $\log ft = 12.3478(23)$ . The spectrum shape was found to be very sensitive to the effective value of the axial-vector coupling constant, and the best description of the decay led to the quenched coupling constants  $g_V^{\text{eff}} = 0.376(5)$  and  $g_A^{\text{eff}} = 0.574(36)$ . These values are

consistent the ones derived from first forbidden nonunique transitions in [56].

Our  $Q$ -value is five times more precise than the recommended one [17] and shifted by  $-1.8$  keV, which is about two standard deviations of the recommended value. The uncertainty is competitive with Penning trap measurements and we call for a confirmation of our  $Q$ -value using this method. Beyond MMCs, the active Array of Cryogenic Calorimeters to Evaluate Spectral Shapes (ACCESS) project aims to measure forbidden  $\beta$  decays such as  $^{99}\text{Tc}$  using an array of neutron transmutation-doped germanium (Ge-NTD or NTD) detectors [73]. Our results could then be confirmed in the near future with another independent technique.

## ACKNOWLEDGMENTS

This work is part of the project 20FUN04 PrimA-LTD that has received funding from the EMPIR programme co-financed by the Participating States and from the European Union's Horizon 2020 research and innovation programme. The Linux-Compute-Cluster at the PTB Berlin was used to run EGSNRC. We thank Rolf Behrens, Gerd Lindner, Andreas Lübbert, and Hayo Zutz for their helpful cooperation.

- 
- [1] K. Kossert and X. Mougeot, The importance of the beta spectrum calculation for accurate activity determination of  $^{63}\text{Ni}$  by means of liquid scintillation counting, *Appl. Radiat. Isot.* **101**, 40 (2015).
- [2] K. E. Koehler, Low temperature microcalorimeters for decay energy spectroscopy, *Appl. Sci.* **11**, 4044 (2021).
- [3] R. P. Fitzgerald, B. K. Alpert, D. T. Becker, D. E. Bergeron, R. M. Essex, K. Morgan, S. Nour, G. O'Neil, D. R. Schmidt, G. A. Shaw *et al.*, Toward a new primary standardization of radionuclide massic activity using microcalorimetry and quantitative milligram-scale samples, *J. Res. Natl. Inst. Stand. Technol.* **126**, 126048 (2021).
- [4] X. Mougeot, Reliability of usual assumptions in the calculation of  $\beta$  and  $\nu$  spectra, *Phys. Rev. C* **91**, 055504 (2015).
- [5] L. Hayen, J. Kostensalo, N. Severijns, and J. Suhonen, First-forbidden transitions in the reactor anomaly, *Phys. Rev. C* **100**, 054323 (2019).
- [6] V. Brdar, R. Plestid, and N. Rocco, Empirical capture cross sections for cosmic neutrino detection with  $^{151}\text{Sm}$  and  $^{171}\text{Tm}$ , *Phys. Rev. C* **105**, 045501 (2022).
- [7] X. Mougeot and C. Bisch, Consistent calculation of the screening and exchange effects in allowed  $\beta^-$  transitions, *Phys. Rev. A* **90**, 012501 (2014).
- [8] J. Kostensalo and J. Suhonen,  $g_a$ -driven shapes of electron spectra of forbidden  $\beta$  decays in the nuclear shell model, *Phys. Rev. C* **96**, 024317 (2017).
- [9] A. Algora, J. Tain, B. Rubio, M. Fallot, and W. Gelletly, Beta-decay studies for applied and basic nuclear physics, *Eur. Phys. J. A* **57**, 85 (2021).
- [10] M. Loidl, J. Beyer, L. Bockhorn, C. Enss, D. Györi, S. Kempf, K. Kossert, R. Mariam, O. Nähle, M. Paulsen, M. Rodrigues, and M. Schmidt, MetroBeta: Beta spectrometry with metallic magnetic calorimeters in the framework of the european program of ionizing radiation metrology, *J. Low Temp. Phys.* **193**, 1251 (2018).
- [11] M.-M. Bé, V. Chisté, C. Dulieu, X. Mougeot, V. Chechev, N. Kuzmenko, F. Kondev, A. Luca, M. Galán, A. Nichols, A. Arinc, A. Pearce, X. Huang, and B. Wang, *Table of Radionuclides*, Monographie BIPM-5, Vol. 6 (Bureau International des Poids et Mesures, Pavillon de Breteuil, F-92310 Sèvres, France, 2011).
- [12] L. Feldman and C. S. Wu, Investigation of the beta-spectra of  $^{10}\text{Be}$ ,  $^{40}\text{K}$ ,  $^{99}\text{Tc}$ , and  $^{36}\text{Cl}$ , *Phys. Rev.* **87**, 1091 (1952).
- [13] S. I. Taimuty, The beta-spectrum of  $^{99}\text{Tc}$ , *Phys. Rev.* **81**, 461 (1951).
- [14] R. E. Snyder and G. B. Beard, Decay of  $^{94}\text{Nb}$  and  $^{94m}\text{Nb}$ , *Phys. Rev.* **147**, 867 (1966).
- [15] M. Reich and H. M. Schüpferling, Formfaktor des  $\beta$ -Spektrums von  $^{99}\text{Tc}$ , *Z. Phys.* **271**, 107 (1974).
- [16] H. Behrens and L. Szybisz, *Shapes of Beta Spectra*, *Physics Data* (Zentralstelle für Atomkernenergie-Dokumentation, 1976).
- [17] M. Wang, W. Huang, F. Kondev, G. Audi, and S. Naimi, The AME2020 atomic mass evaluation (II). Tables, graphs and references, *Chin. Phys. C* **45**, 030003 (2021).
- [18] D. E. Alburger, P. Richards, and T. H. Ku, Beta decay of  $^{99}\text{Tc}^m$ , *Phys. Rev. C* **21**, 705 (1980).
- [19] H. R. Doran, A. J. Cresswell, D. C. W. Sanderson, and G. Falcone, Nuclear data evaluation for decay heat analysis of spent nuclear fuel over 1–100 k year timescale, *Eur. Phys. J. Plus* **137**, 665 (2022).
- [20] M. Loidl, J. Beyer, L. Bockhorn, C. Enss, S. Kempf, K. Kossert, R. Mariam, O. Nähle, M. Paulsen, P. Ranitzsch, M. Rodrigues, and M. Schmidt, Beta spectrometry with metallic magnetic calorimeters in the framework of the European EMPIR project MetroBeta, *Appl. Radiat. Isot.* **153**, 108830 (2019).

- [21] M. Loidl, J. Beyer, L. Bockhorn, J. J. Bonaparte, C. Enss, S. Kempf, K. Kossert, R. Mariam, O. Nähle, M. Paulsen, P. Ranitzsch, M. Rodrigues, and M. Wegner, Precision measurements of beta spectra using metallic magnetic calorimeters within the European metrology research project metrobeta, *J. Low Temp. Phys.* **199**, 451 (2020).
- [22] A. Fleischmann, C. Enss, and G. Seidel, Metallic magnetic calorimeters, in *Cryogenic Particle Detection: Topics in Applied Physics*, edited by C. Enss (Springer, Berlin, 2005), pp. 151–216.
- [23] A. Fleischmann, L. Gastaldo, S. Kempf, A. Kirsch, A. Pabinger, C. Pies, J. Porst, P. Ranitzsch, S. Schäfer, F. v. Seggern, T. Wolf, C. Enss, and G. M. Seidel, Metallic magnetic calorimeters, *AIP Conf. Proc.* **1185**, 571 (2009).
- [24] S. Kempf, A. Fleischmann, L. Gastaldo, and C. Enss, Physics and applications of metallic magnetic calorimeters, *J. Low Temp. Phys.* **193**, 365 (2018).
- [25] D. Drung, C. Aßmann, J. Beyer, A. Kirste, M. Peters, F. Ruede, and T. Schurig, Highly sensitive and easy-to-use SQUID sensors, *IEEE Trans. Appl. Supercond.* **17**, 699 (2007).
- [26] H. Rotzinger, M. Linck, A. Burck, M. Rodrigues, M. Loidl, E. Leblanc, L. Fleischmann, A. Fleischmann, and C. Enss, Beta spectrometry with magnetic calorimeters, *J. Low Temp. Phys.* **151**, 1087 (2008).
- [27] M. Loidl, M. Rodrigues, C. Le-Bret, and X. Mougeot, Beta spectrometry with metallic magnetic calorimeters, *Appl. Radiat. Isot.* **87**, 302 (2014).
- [28] M. Paulsen, J. Beyer, L. Bockhorn, C. Enss, S. Kempf, K. Kossert, M. Loidl, R. Mariam, O. Nähle, P. Ranitzsch, and M. Rodrigues, Development of a beta spectrometry setup using metallic magnetic calorimeters, *J. Instrum.* **14**, P08012 (2019).
- [29] M. Paulsen, High resolution beta spectrometry with metallic magnetic calorimeters for radionuclide metrology, Ph.D. thesis, Heidelberg University (2022).
- [30] E. Mausolf, F. Poineau, T. Hartmann, J. Droessler, and K. Czerwinski, Characterization of electrodeposited technetium on gold foil, *J. Electrochem. Soc.* **158**, E32 (2011).
- [31] The MathWorks Inc., *MATLAB* version: 9.2.0 (R2017a) (The MathWorks Inc., Natick, Massachusetts, United States, 2017).
- [32] M.-M. Bé, V. Chisté, C. Dulieu, E. Browne, V. Chechev, N. Kuzmenko, R. Helmer, A. Nichols, E. Schönfeld, and R. Dersch, *Table of Radionuclides*, Monographie BIPM-5, Vol. 1 (Bureau International des Poids et Mesures, Pavillon de Breteuil, F-92310 Sèvres, France, 2004).
- [33] R. D. Deslattes, E. G. Kessler Jr, P. Indelicato, L. De Billy, E. Lindroth, and J. Anton, X-ray transition energies: New approach to a comprehensive evaluation, *Rev. Mod. Phys.* **75**, 35 (2003).
- [34] L. Bockhorn, M. Paulsen, J. Beyer, K. Kossert, M. Loidl, O. J. Nähle, P. C.-O. Ranitzsch, and M. Rodrigues, Improved source/absorber preparation for radionuclide spectrometry based on low-temperature calorimetric detectors, *J. Low Temp. Phys.* **199**, 298 (2020).
- [35] G. Van Rossum, and F. L. Drake Jr., Python tutorial (Centrum voor Wiskunde en Informatica Amsterdam, The Netherlands, 1995).
- [36] P. T. Boggs and J. E. Rogers, Orthogonal distance regression, in *Proceedings of the AMS-IMS-SIAM Joint Summer Research Conference on Statistical Analysis of Measurement Error Models and Applications*, edited by P. J. Brown and W. A. Fuller (American Mathematical Society, Providence, Rhode Island, 1990), Vol. 112, pp. 183–194.
- [37] C. Bates, C. Pies, S. Kempf, D. Hengstler, A. Fleischmann, L. Gastaldo, C. Enss, and S. Friedrich, Reproducibility and calibration of MMC-based high-resolution gamma detectors, *Appl. Phys. Lett.* **109**, 023513 (2016).
- [38] P. Bell, E. Burovski, J. Charlong, R. Gommers, M. Picus, T. Reddy, P. Roy, S. Wallkötter, and A. Volant, *Orthogonal Distance Regression in Python's SciPy 1.7.1 Module* (The SciPy Community, 2021).
- [39] M.-M. Bé, V. Chisté, C. Dulieu, M. Kellett, X. Mougeot, A. Arinc, V. Chechev, N. Kuzmenko, T. Kibédi, A. Luca, and A. Nichols, *Table of Radionuclides*, Monographie BIPM-5, Vol. 8 (Bureau International des Poids et Mesures, Pavillon de Breteuil, F-92310 Sèvres, France, 2016).
- [40] M.-M. Bé, V. Chisté, C. Dulieu, M. Kellett, X. Mougeot, A. Arinc, V. Chechev, N. Kuzmenko, T. Kibédi, A. Luca, and A. Nichols, *Table of Radionuclides*, Monographie BIPM-5, Vol. 9 (unpublished).
- [41] M. Paulsen, K. Kossert, and J. Beyer, An unfolding algorithm for high resolution microcalorimetric beta spectrometry, *Nucl. Instrum. Methods Phys. Res. Sect. A* **953**, 163128 (2020).
- [42] I. Kawrakow, D. W. O. Rogers, E. Mainegra-Hing, F. Tessier, R. W. Townson, and B. R. B. Walters, *EGSnrc toolkit for Monte Carlo Simulation of Ionizing Radiation Transport* (National Research Council Canada, 2021).
- [43] C. Bisch, *Etude de la forme des spectres  $\beta$* , Ph.D. thesis, Université de Strasbourg, 2014.
- [44] A. Singh, Metrological study of the shape of beta spectra and experimental validation of theoretical models, Ph.D. thesis, Université de Strasbourg, 2020.
- [45] A. Singh, X. Mougeot, B. Sabot, D. Lacour, and A. Nourredine, Beta spectrum measurements using a quasi- $4\pi$  detection system based on Si detectors, *Appl. Radiat. Isot.* **154**, 108897 (2019).
- [46] A. Singh, X. Mougeot, B. Sabot, D. Lacour, and A.-M. Nourredine, Experimental study of  $\beta$  spectra using Si detectors, in *EPJ Web of Conferences* (EDP Sciences, Les Ulis, France, 2020), Vol. 239, p. 02001.
- [47] Computer code labZY nanoMCA module, Yantel (Yantel, LLC, Los Alamos, NM, USA, 2022), <https://www.yantel.com/products/nanomca/>.
- [48] A. Singh, X. Mougeot, S. Leblond, M. Loidl, B. Sabot, and A. Nourredine, Development of a  $4\pi$  detection system for the measurement of the shape of  $\beta$  spectra, *Nucl. Instrum. Methods Phys. Res. Sect. A* **1053**, 168354 (2023).
- [49] R. Brun and F. Rademakers, ROOT—An object oriented data analysis framework, *Nucl. Instrum. Methods Phys. Res. Sect. A* **389**, 81 (1997).
- [50] F. Salvat, J. Fernandez-Varea, and J. Sempau, *PENELOPE-2014: A Code System for Monte Carlo Simulation of Electron and Photon Transport* (OECD/NEA Data Bank, NEA/NSC/DOC 3, Issy-les-Moulineaux, France, 2015).
- [51] K. Kossert, M. Loidl, X. Mougeot, M. Paulsen, P. Ranitzsch, and M. Rodrigues, High precision measurement of the  $^{151}\text{Sm}$  beta decay by means of a metallic magnetic calorimeter, *Appl. Radiat. Isot.* **185**, 110237 (2022).
- [52] L. Hayen, N. Severijns, K. Bodek, D. Rozpedzik, and X. Mougeot, High precision analytical description of the allowed  $\beta$  spectrum shape, *Rev. Mod. Phys.* **90**, 015008 (2018).



- [53] J. C. Hardy and I. S. Towner, Superallowed  $0^+ \rightarrow 0^+$  nuclear  $\beta$  decays: A new survey with precision tests of the conserved vector current hypothesis and the standard model, *Phys. Rev. C* **79**, 055502 (2009).
- [54] F. N. D. Kurie, J. R. Richardson, and H. C. Paxton, The radiations emitted from artificially produced radioactive substances. I. The upper limits and shapes of the  $\beta$ -ray spectra from several elements, *Phys. Rev.* **49**, 368 (1936).
- [55] R. L. Workman *et al.* (Particle Data Group), Review of particle physics, *Prog. Theor. Exp. Phys.* **2022**, 083C01 (2022).
- [56] J. T. Suhonen, Value of the axial-vector coupling strength in  $\beta$  and  $\beta\beta$  decays: A review, *Frontier. Phys.* **5**, 55 (2017).
- [57] P. Gysbers, G. Hagen, J. D. Holt, G. R. Jansen, T. D. Morris, P. Navrátil, T. Papenbrock, S. Quaglioni, A. Schwenk, S. R. Stroberg, and K. A. Wendt, Discrepancy between experimental and theoretical  $\beta$ -decay rates resolved from first principles, *Nat. Phys.* **15**, 428 (2019).
- [58] M. Haaranen, P. C. Srivastava, and J. Suhonen, Forbidden nonunique  $\beta$  decays and effective values of weak coupling constants, *Phys. Rev. C* **93**, 034308 (2016).
- [59] J. Kostensalo, M. Haaranen, and J. Suhonen, Electron spectra in forbidden  $\beta$  decays and the quenching of the weak axial-vector coupling constant  $g_A$ , *Phys. Rev. C* **95**, 044313 (2017).
- [60] F. G. A. Quarati, G. Bollen, P. Dorenbos, M. Eibach, K. Gulyuz, A. Hamaker, C. Izzo, D. K. Keblbeck, X. Mougeot, D. Puentes, M. Redshaw, R. Ringle, R. Sandler, J. Surbrook, and I. Yandow, Measurements and computational analysis of the natural decay of  $^{176}\text{Lu}$ , *Phys. Rev. C* **107**, 024313 (2023).
- [61] H. Behrens and W. Bühring, *Electron Radial Wave Functions and Nuclear Beta-decay* (Clarendon Press, Oxford, 1982).
- [62] N. C. Pyper and M. R. Harston, Atomic effects on  $\beta$ -decays, *Proc. R. Soc. London A* **420**, 277 (1988).
- [63] X. Mougeot, Atomic exchange correction in forbidden unique beta transitions, *Appl. Radiat. Isot.* **201**, 111018 (2023).
- [64] M. Haaranen, J. Kotila, and J. Suhonen, Spectrum-shape method and the next-to-leading-order terms of the  $\beta$ -decay shape factor, *Phys. Rev. C* **95**, 024327 (2017).
- [65] B. Brown and W. Rae, The Shell-Model Code NuShellX@MSU, *Nucl. Data Sheets* **120**, 115 (2014).
- [66] D. Gloeckner, Shell-model systematics of the zirconium and niobium isotopes, *Nucl. Phys. A* **253**, 301 (1975).
- [67] H. Mach, E. K. Warburton, R. L. Gill, R. F. Casten, J. A. Becker, B. A. Brown, and J. A. Winger, Meson-exchange enhancement of the first-forbidden  $^{96}\text{Y}^g(0^-) \rightarrow ^{96}\text{Zr}^g(0^+)$   $\beta$  transition:  $\beta$  decay of the low-spin isomer of  $^{96}\text{Y}$ , *Phys. Rev. C* **41**, 226 (1990).
- [68] A. F. Lisetskiy, B. A. Brown, M. Horoi, and H. Grawe, New  $T = 1$  effective interactions for the  $f_{5/2} p_{3/2} p_{1/2} g_{9/2}$  model space: Implications for valence-mirror symmetry and seniority isomers, *Phys. Rev. C* **70**, 044314 (2004).
- [69] R. Sadler and H. Behrens, Second-forbidden beta-decay and the effect of (V+A)- and S-interaction admixtures:  $^{36}\text{Cl}$ , *Z. Phys. A* **346**, 25 (1993).
- [70] J. Damgaard and A. Winter, Use of conserved vector current theory in first forbidden  $\beta$ -decay, *Phys. Lett.* **23**, 345 (1966).
- [71] M. Ramalho and J. Suhonen, Shell-model treatment of the  $\beta$  decay of  $^{99}\text{Tc}$ , [arXiv:2312.07448](https://arxiv.org/abs/2312.07448).
- [72] O. Nițescu, S. Stoica, and F. Šimkovic, Exchange correction for allowed  $\beta$  decay, *Phys. Rev. C* **107**, 025501 (2023).
- [73] L. Pagnanini, G. Benato, P. Carniti, E. Celi, D. Chiesa, J. Corbett, I. Dafinei, S. Di Domizio, P. Di Stefano, S. Ghislandi *et al.*, Array of cryogenic calorimeters to evaluate the spectral shape of forbidden  $\beta$ -decays: The ACCESS project, *Eur. Phys. J. Plus* **138**, 445 (2023).